Real-time solution of computational problems using databases of parametric linear reduced-order models with arbitrary underlying meshes

David Amsallem[a,], Radek Tezaur[a], Charbel Farhat[b]

[a]*Department of Aeronautics and Astronautics, Durand Building, 496 Lomita Mall. Stanford University, Stanford, 94305-4035, USA*

[b]*Department of Aeronautics and Astronautics, Institute for Computational and Mathematical Engineering, Department of Mechanical Engineering. Stanford University, Mail Code 4035, Stanford, CA 94305, U.S.A.*

Abstract

A comprehensive approach for real-time computations using a database of parameterized linear reduced-order models (ROMs) is proposed. The method proceeds by sampling offline ROMs for specific values of the parameters and interpolating online the associated reduced operators. In the offline phase, a pre-processing step transforms the reduced operators into consistent sets of generalized coordinates prior to their interpolation. The present paper also introduces a consistency enforcement approach for models defined on arbitrary underlying meshes. In the online phase, the operators are interpolated on matrix manifolds. The proposed framework is illustrated on two realistic multi-physics problems: an inverse acoustic scattering problem around a submarine and flutter predictions for a wing-tank system. The second application is implemented on a mobile device, illustrating the capability of the proposed framework to operate in real-time.

Keywords: Parametric model order reduction, database, interpolation, mobile computing, aeroelasticity, acoustic scattering

1. Introduction

Many engineering applications require the ability to generate predictions of the behavior of physical systems in real-time. Among those applications, one can mention design optimization, optimal control, the solution of inverse problems as well as uncertainty quantification. All of these applications require a large number of predictions for varying values of operating conditions. The operating conditions, usually described by a set of parameters, may define boundary conditions, initial conditions, physical or shape parameters that define the problem of interest and its underlying differential equations. However, each of these predictions usually demands computationally intensive calculations as accurate discretization of the underlying differential equations often leads to large scale systems of equations.

Projection-based model reduction [1, 2] reduces the large computational cost associated with each solution of the underlying high-dimensional model (HDM) by reducing the number of degrees of freedom in the computation. For this purpose, a reduced-order basis (ROB) is defined and the solution is restricted to the subspace described by the ROB. The current most challenging model reduction problems are those associated with nonlinear systems and parameter variations. Nonlinear systems require additional levels of approximation to enable large computational speedups [3, 4, 5, 6, 7, 8]. The model reduction of parameterized systems is also challenging due to the non-robustness of reduced-order model with respect to parameter variations that requires an appropriate offline training phase [9, 10, 11, 12]. Approaches addressing the

Email addresses: amsallem@stanford.edu (David Amsallem), rtezaur@stanford.edu (Radek Tezaur), cfarhat@stanford.edu (Charbel Farhat)

URL: stanford.edu/∼amsallem (David Amsallem)

model reduction of nonlinear parameterized systems are proposed in [13, 14, 15, 16]. The focus of the present paper is on the efficient model reduction of linear parameterized systems.

More specifically, for linear parameterized systems, database approaches can be developed by pre-computing in an offline phase the reduced linear operators of a common reduced dimension for specific values of the parameters [10, 17, 18, 11, 19, 20, 21].These linear operators are subsequently interpolated in the online phase for values of the parameters not present in the database. The small dimensionality of the reduced operators leads to real-time interpolation and predictions on-the-fly.

The interpolation of local reduced operators is however a challenging because each reduced operator is written in terms of a distinct set of generalized coordinates corresponding to the local ROBs associated with each reduced-order model (ROM). To address this issue, approaches based on congruent transformations are proposed in [18, 20, 21] when the underlying HDMs are defined on a common mesh. These approaches cannot, however, be applied when each HDM is defined on a different mesh. The present paper introduces a novel approach, also based on congruent transformations, that addresses the challenge associated with arbitrary underlying meshes.

Special care is also given in this paper to the interpolation step of the proposed procedure. The preservation of properties associated with the linear reduced operators can indeed be enforced by interpolating these operators on appropriate matrix manifolds [10, 17, 18, 19, 21]. In that case, after appropriately mapping the reduced operators, interpolation can be carried out in the tangent space to the matrix manifold. As such, as long as the interpolation procedure preserves the tangent space, the interpolated quantity will also belong to the tangent space and can be mapped back to the manifold, leading to an interpolated reduced quantity that preserves its properties.

This paper is organized as follows. The problem of interest and the ROM database approach are formulated in Section 2. The issue of consistency of reduced-order operators and its enforcement in the case of common and arbitrary underlying meshes are then investigated in Section 3. The interpolation of the resulting consistent database of ROMs is developed in Section 4. Special care is given to the sampling, storage and exploitation of the database. The proposed approach is applied in Section 5 to the model reduction of two parameterized systems. The first one is the analysis of a parameterized acoustic scattering system defined on arbitrary underlying meshes. In that case, the database approach is applied to the online solution of inverse problems. The second problem is the real-time flutter analysis of an aeroelastic system for flight conditions ranging from the subsonic to supersonic regimes. It is shown that the proposed approach successfully enables real-time predictions on a mobile device. Finally, conclusions are given in Section 6.

2. Problem formulation and solution approach

In this paper, linear-time invariant parametric (LTIP) systems of one of the following two forms are considered

1. First-order LTIP systems of the form

$$\mathbf{E}(\boldsymbol{\mu})\frac{d\mathbf{w}}{dt}(t) = \mathbf{A}(\boldsymbol{\mu})\mathbf{w}(t) + \mathbf{B}(\boldsymbol{\mu})\mathbf{u}(t) \tag{1}$$

and their formulation in the frequency domain

$$(j\omega\mathbf{E}(\boldsymbol{\mu}) - \mathbf{A}(\boldsymbol{\mu}))\mathbf{w}(\omega) = \mathbf{B}(\boldsymbol{\mu})\mathbf{u}(\omega). \tag{2}$$

The high-dimensional state vector is $\mathbf{w} \in \mathbb{R}^N$, $j^2 = -1$, $t \geq 0$ denotes time and $\omega \geq 0$ frequency. $\mathbf{E}$ and $\mathbf{A}$ are square high-dimensional matrices of dimension N. $\mathbf{u} \in \mathbb{R}^{N_i}$ denotes the input variable of dimension $N_i \ll N$ and $\mathbf{B} \in \mathbb{R}^{N\times N_i}$. All operators depend on a vector of $N_{\boldsymbol{\mu}}$ parameters $\boldsymbol{\mu} \in \mathcal{D} \subset \mathbb{R}^{N_{\boldsymbol{\mu}}}$.

For both formulations, an output quantity of interest $\mathbf{y} \in \mathbb{R}^{N_o}$ is defined as

$$\mathbf{y} = \mathbf{G}(\boldsymbol{\mu})\mathbf{w} + \mathbf{H}(\boldsymbol{\mu})\mathbf{u}, \tag{3}$$

with $N_o \ll N$ and $\mathbf{G} \in \mathbb{R}^{N_o\times N}$ and $\mathbf{H} \in \mathbb{R}^{N_o\times N_i}$.

2. Second-order LTIP systems of the form

$$\mathbf{M}(\boldsymbol{\mu})\frac{d^2\mathbf{w}}{dt^2}(t) + \mathbf{C}(\boldsymbol{\mu})\frac{d\mathbf{w}}{dt}(t) + \mathbf{K}(\boldsymbol{\mu})\mathbf{w}(t) = \mathbf{B}(\boldsymbol{\mu})\mathbf{u}(t) \tag{4}$$

and their equivalent formulation in the frequency domain are considered

$$(-\omega^2\mathbf{M}(\boldsymbol{\mu}) + j\omega\mathbf{C}(\boldsymbol{\mu}) + \mathbf{K}(\boldsymbol{\mu}))\mathbf{w}(\omega) = \mathbf{B}(\boldsymbol{\mu})\mathbf{u}(\omega). \tag{5}$$

$\mathbf{M}$, $\mathbf{C}$ and $\mathbf{K}$ are also parameter-dependent square linear operators of dimension N. For both formulations, an output quantity of interest $\mathbf{y}$ can be defined as in (3).

The problem of interest is the fast computation of the output $\mathbf{y}$ for a given value of the parameters $\boldsymbol{\mu} \in \mathcal{D}$. More specifically, the computational cost associated with these computations should not scale with N anymore.

To address this problem, an approach based on a database of linear projection-based ROMs is considered. This approach proceeds in two steps.

1. In the first offline step, N_{DB} sample parameter values $\{\boldsymbol{\mu}_i\}_{i=1}^{N_{\text{DB}}} \in \mathcal{D} \subset \mathbb{R}^{N_\mu}$ are selected and ROMs are constructed for each parameter value by defining right and left reduced-order bases (ROBs) $\mathbf{V}(\boldsymbol{\mu}) \in \mathbb{R}^{N\times k}$ and $\mathbf{W}(\boldsymbol{\mu}) \in \mathbb{R}^{N\times k}$, $k \ll N$ and approximating the state $\mathbf{w}$ as $\mathbf{w} \approx \mathbf{V}(\boldsymbol{\mu})\mathbf{q}$ where $\mathbf{q} \in \mathbb{R}^k$ is either solution of a reduced LTIP system in the time domain or frequency domain, as detailed below. The output equation in terms of the reduced variable $\mathbf{q}$ is then

$$\mathbf{y}_r = \mathbf{G}_r(\boldsymbol{\mu})\mathbf{q} + \mathbf{H}(\boldsymbol{\mu})\mathbf{u} \tag{6}$$

with $\mathbf{G}_r(\boldsymbol{\mu}) = \mathbf{G}(\boldsymbol{\mu})\mathbf{V}(\boldsymbol{\mu}) \in \mathbb{R}^{N_o\times k}$.

   (a) For first-order LTIP systems, the reduced equations in the time-domain are

$$\mathbf{E}_r(\boldsymbol{\mu})\frac{d\mathbf{q}}{dt}(t) = \mathbf{A}_r(\boldsymbol{\mu})\mathbf{q}(t) + \mathbf{B}_r(\boldsymbol{\mu})\mathbf{u}(t) \tag{7}$$

   and in the frequency domain

$$(j\omega\mathbf{E}_r(\boldsymbol{\mu}) - \mathbf{A}_r(\boldsymbol{\mu}))\mathbf{q}(\omega) = \mathbf{B}_r(\boldsymbol{\mu})\mathbf{u}(\omega). \tag{8}$$

   where $\mathbf{E}_r(\boldsymbol{\mu}) = \mathbf{W}(\boldsymbol{\mu})^T\mathbf{E}(\boldsymbol{\mu})\mathbf{V}(\boldsymbol{\mu}) \in \mathbb{R}^{k\times k}$, $\mathbf{A}_r(\boldsymbol{\mu}) = \mathbf{W}(\boldsymbol{\mu})^T\mathbf{A}(\boldsymbol{\mu})\mathbf{V}(\boldsymbol{\mu}) \in \mathbb{R}^{k\times k}$ and $\mathbf{B}_r(\boldsymbol{\mu}) = \mathbf{W}(\boldsymbol{\mu})^T\mathbf{B}(\boldsymbol{\mu}) \in \mathbb{R}^{k\times N_i}$.

   (b) For second-order LTIP systems, the time-domain reduced equations are

$$\mathbf{M}_r(\boldsymbol{\mu})\frac{d^2\mathbf{q}}{dt^2}(t) + \mathbf{C}_r(\boldsymbol{\mu})\frac{d\mathbf{q}}{dt}(t) + \mathbf{K}_r(\boldsymbol{\mu})\mathbf{q}(t) = \mathbf{B}_r(\boldsymbol{\mu})\mathbf{u}(t) \tag{9}$$

   where $\mathbf{M}_r(\boldsymbol{\mu}) = \mathbf{W}(\boldsymbol{\mu})^T\mathbf{M}(\boldsymbol{\mu})\mathbf{V}(\boldsymbol{\mu})$, $\mathbf{C}_r(\boldsymbol{\mu}) = \mathbf{W}(\boldsymbol{\mu})^T\mathbf{C}(\boldsymbol{\mu})\mathbf{V}(\boldsymbol{\mu})$ and $\mathbf{K}_r(\boldsymbol{\mu}) = \mathbf{W}(\boldsymbol{\mu})^T\mathbf{K}(\boldsymbol{\mu})\mathbf{V}(\boldsymbol{\mu})$ are square reduced operators of dimension k. The reduced equations in the frequency domain are

$$(-\omega^2\mathbf{M}_r(\boldsymbol{\mu}) + j\omega\mathbf{C}_r(\boldsymbol{\mu}) + \mathbf{K}_r(\boldsymbol{\mu}))\mathbf{q}(\omega) = \mathbf{B}_r(\boldsymbol{\mu})\mathbf{u}(\omega). \tag{10}$$

   There are several model reduction techniques that can be applied to construct the ROBs $\mathbf{W}(\boldsymbol{\mu})$ and $\mathbf{V}(\boldsymbol{\mu})$ for LTI systems. Among those, the most popular are proper orthogonal decomposition (POD) [2, 22], balanced truncation [1] and moment matching [23, 24].

   Once the reduced operators are computed for the sampled values of the parameters, these reduced matrices are stored in a database of the form

$$\mathcal{DB} = \{\boldsymbol{\mu}_i, (\mathbf{E}_r(\boldsymbol{\mu}_i), \mathbf{A}_r(\boldsymbol{\mu}_i), \mathbf{B}_r(\boldsymbol{\mu}_i), \mathbf{G}_r(\boldsymbol{\mu}_i), \mathbf{H}(\boldsymbol{\mu}_i))\}_{i=1}^{N_{\text{DB}}} \tag{11}$$

for first-order systems and

$$\mathcal{DB} = \{\boldsymbol{\mu}_i, (\mathbf{M}_r(\boldsymbol{\mu}_i), \mathbf{C}_r(\boldsymbol{\mu}_i), \mathbf{K}_r(\boldsymbol{\mu}_i), \mathbf{B}_r(\boldsymbol{\mu}_i), \mathbf{G}_r(\boldsymbol{\mu}_i), \mathbf{H}(\boldsymbol{\mu}_i))\}_{i=1}^{N_{\text{DB}}} \tag{12}$$

for second-order systems.

In this work, the left and right ROBs are assumed to have orthonormal columns with respect to a common symmetric positive definite matrix $\boldsymbol{\mathcal{M}}$, that is $\mathbf{W}(\boldsymbol{\mu})^T \boldsymbol{\mathcal{M}} \mathbf{W}(\boldsymbol{\mu}) = \mathbf{I}_k$ and $\mathbf{V}(\boldsymbol{\mu})^T \boldsymbol{\mathcal{M}} \mathbf{V}(\boldsymbol{\mu}) = \mathbf{I}_k$. This property can be easily enforced a posteriori by applying a Gram-Schmidt orthogonalization procedure to the columns of non-orthonormal ROBs or directly in the ROB construction procedure [25].

2. In the online phase, for a given value $\boldsymbol{\mu}^\star \in \mathcal{D}$ of the parameters, reduced operators are constructed by interpolation of the elements of the database $\mathcal{DB}$.

Two technical issues however arise in the online interpolation step associated with the proposed approach:

1. The reduced quantities are not defined in the same system of reduced coordinates. Indeed, for each parameter $\boldsymbol{\mu}_i$, the system of reduced coordinates is defined by the local ROBs $\mathbf{V}(\boldsymbol{\mu}_i)$ and $\mathbf{W}(\boldsymbol{\mu}_i)$. A naive interpolation of the reduced operators may result in interpolation quantities that are not consistent with each other. A comprehensive approach to address this issue is proposed in Section 3

2. The linear operators stored in the database $\mathcal{DB}$ may have properties that should be preserved by interpolation. An approach relying on interpolation on a matrix manifold has been proposed in [17, 21] to preserve these properties. The approach is briefly recalled and extended in Section 4.

3. Consistency between reduced-order models

3.1. Concept

As underlined in the previous section and in [21], the fact that local reduced operators are defined in different sets of generalized coordinates prevents their direct interpolation. In this paper, two approaches are presented to address this issue. Both rely on a congruence transformation of the reduced operators to enforce consistency. They recognize the fact that the choice of local ROBs is not unique. Indeed, for a given right ROB $\mathbf{V}(\boldsymbol{\mu})$, any ROB of the form $\mathbf{V}(\boldsymbol{\mu})\mathbf{Q}$ with $\mathbf{Q}^T\mathbf{Q} = \mathbf{I}_k$ defines an equally valid coordinate representation for the same ROM [21] with $\boldsymbol{\mathcal{M}}$-orthogonal columns. Similarly, for the left ROB $\mathbf{W}(\boldsymbol{\mu})$, any left ROB of the form $\mathbf{W}(\boldsymbol{\mu})\mathbf{Z}$ with $\mathbf{Z}^T\mathbf{Z} = \mathbf{I}_k$ defines an equally valid basis.

In turn, for a given first-order LTI ROM $\mathcal{R} = (\mathbf{E}_r, \mathbf{A}_r, \mathbf{B}_r, \mathbf{G}_r, \mathbf{H})$, an equivalence class of ROMs under left and right multiplications by orthogonal matrices $\mathbf{Z}$ and $\mathbf{Q}$ can be defined as

$$\mathcal{C}(\mathcal{R}) = \left\{ \left(\mathbf{Z}^T\mathbf{E}_r\mathbf{Q}, \mathbf{Z}^T\mathbf{A}_r\mathbf{Q}, \mathbf{Z}^T\mathbf{B}_r, \mathbf{G}_r\mathbf{Q}, \mathbf{H}\right) \text{ such that } \mathbf{Z}^T\mathbf{Z} = \mathbf{I},\ \mathbf{Q}^T\mathbf{Q} = \mathbf{I} \right\}. \tag{13}$$

Similarly, for a second-order LTI ROM $\mathcal{R} = (\mathbf{M}_r, \mathbf{C}_r, \mathbf{K}_r, \mathbf{B}_r, \mathbf{G}_r, \mathbf{H})$, the equivalence class of ROMs under left and right multiplications by orthogonal matrices $\mathbf{Z}$ and $\mathbf{Q}$ is

$$\mathcal{C}(\mathcal{R}) = \left\{ \left(\mathbf{Z}^T\mathbf{M}_r\mathbf{Q}, \mathbf{Z}^T\mathbf{C}_r\mathbf{Q}, \mathbf{Z}^T\mathbf{K}_r\mathbf{Q}, \mathbf{Z}^T\mathbf{B}_r, \mathbf{G}_r\mathbf{Q}, \mathbf{H}\right) \text{ such that } \mathbf{Z}^T\mathbf{Z} = \mathbf{I},\ \mathbf{Q}^T\mathbf{Q} = \mathbf{I} \right\}. \tag{14}$$

Both approaches proposed in this paper will rely on a preprocessing step for which optimal transformations $\mathbf{Q}^\star(\boldsymbol{\mu}_i)$ and $\mathbf{Z}^\star(\boldsymbol{\mu}_i)$, $i = 1, \cdots, N_{\text{DB}}$ are applied to the N_{DB} ROMs stored in the database $\mathcal{DB}$.

The first approach, originally introduced in [21] and described in Section 3.2 is applicable whenever the underlying HDMs are defined on the same reference mesh. The location of the mesh nodes is potentially parameter dependent but the topology of the mesh is common to all parameter values. This requirement is relaxed in Section 3.3 where a novel approach is introduced to enforce consistency in the case of arbitrary meshes. In that case, each HDM can have a different number of dofs.

A word of caution should however be formulated regarding interpolation of reduced linear operators. There are cases for which consistency cannot be enforced. Consider for instance the case of two configurations

$\boldsymbol{\mu}_1$ and $\boldsymbol{\mu}_2$ associated with a common mesh and for which the right ROBs $\mathbf{V}(\boldsymbol{\mu}_1)$ and $\mathbf{V}(\boldsymbol{\mu}_2)$ are orthogonal to each other. In that case, the subspaces respectively defined by the ROBs are orthogonal as well and no transformation of the form $\{\mathbf{V}(\boldsymbol{\mu}_i)\mathbf{Q}(\boldsymbol{\mu}_i)\}_{i=1}^2$ can define a consistent set of reduced coordinates. The degree of consistency between two ROBs will be quantitatively defined in the case of common underlying meshes in Section 3.2 and a truncation procedure introduced to further enforce consistency.

3.2. Enforcement in the case of a common underlying mesh

Consistency can be enforced in the case of a common underlying mesh by solving a series of Procrustes problems [21]. More specifically, given two local right reduced bases $\mathbf{V}_i = \mathbf{V}(\boldsymbol{\mu}_i)$ and $\mathbf{V}_j = \mathbf{V}(\boldsymbol{\mu}_j)$, $\mathbf{V}_j$ can be written in terms of $\mathbf{V}_i$ as

$$\mathbf{V}_j = \mathbf{V}_i\mathbf{R}_{ij} + \mathbf{T}_{ij} \tag{15}$$

where $\mathbf{T}_{ij}$ is the component of $\mathbf{V}_j$ that is $\boldsymbol{\mathcal{M}}$-orthogonal to $\mathbf{V}_i$ i.e. $\mathbf{T}_{ij}^T\boldsymbol{\mathcal{M}}\mathbf{V}_i = \mathbf{0}$.

The subspace angles between the ROBs $\mathbf{V}_i$ and $\mathbf{V}_j$ define a measure of the maximum achievable consistency. The subspace angles can be computed by the following three-step procedure:

1. Form $\mathbf{V}_i^T\boldsymbol{\mathcal{M}}\mathbf{V}_j = \mathbf{R}_{ij}$.
2. Compute a singular value decomposition $\mathbf{R}_{ij} = \mathbf{X}\boldsymbol{\Sigma}\mathbf{Y}^T$ where $\mathbf{X} = [\mathbf{x}_1, \ldots, \mathbf{x}_k]$, $\mathbf{Y} = [\mathbf{y}_1, \ldots, \mathbf{y}_k]$ and $\boldsymbol{\Sigma} = \mathrm{diag}(\sigma_1, \cdots, \sigma_k)$.
3. Compute the subspace angles as $\theta_\ell = \arccos(\sigma_\ell),\ \ell = 1, \cdots, k$. The canonical vectors associated with each angle θ_ℓ are $(\mathbf{V}_i\mathbf{x}_\ell, \mathbf{V}_j\mathbf{y}_\ell)$. Note that the angles are ordered increasingly as $0 \leq \theta_1 \leq \cdots \leq \theta_k \leq \frac{\pi}{2}$.

A subspace angle θ_ℓ that is equal to zero reflects perfect consistency between the associated vectors $\mathbf{V}_i\mathbf{x}_\ell$ and $\mathbf{V}_j\mathbf{y}_\ell$. In general, angles that are greater than a threshold $\theta_{\max} = \frac{\pi}{4}$ may define cases for which consistency cannot be achieved. One option to address this issue that is discussed below is to truncate the directions associated with those large angles. An alternate option is to refine the database until smaller subspace angles are achieved.

For a given database $\mathcal{DB}$, optimal transformations $\{\mathbf{Q}(\boldsymbol{\mu}_i)\}_{i=1}^{N_{\mathrm{DB}}}$ can be computed by fixing one of the ROBs (say $\mathbf{Q}(\boldsymbol{\mu}_{i_0}) = \mathbf{I}_k$) and computing the transformations as the minimizers of the following series of Procrustes problems:

$$\begin{aligned} \mathbf{Q}(\boldsymbol{\mu}_i) = \underset{\mathbf{S}\in\mathbb{R}^{k\times k}}{\mathrm{argmin}} \|\mathbf{V}_i\mathbf{S} - \mathbf{V}_{i_0}\|_{\boldsymbol{\mathcal{M}}}, \quad i = 1, \cdots, N_{\mathrm{DB}}, \\ \text{s.t. } \mathbf{S}^T\mathbf{S} = \mathbf{I}_k, \end{aligned} \tag{16}$$

where $\|\mathbf{N}\|_{\boldsymbol{\mathcal{M}}} = \|\boldsymbol{\mathcal{M}}^{\frac{1}{2}}\mathbf{N}\|_F$. The optimal transformation $\mathbf{Q}(\boldsymbol{\mu}_i)$ can be determined analytically from the SVD of $\mathbf{R}_{ii_0}$ as

$$\mathbf{Q}(\boldsymbol{\mu}_i) = \mathbf{X}\mathbf{Y}^T. \tag{17}$$

As stated above, truncation of the ROBs can be used to enforce consistency. For each ROB $\mathbf{V}_i$, $i = 1, \cdots, N_{\mathrm{DB}}$, the maximum index ℓ_i for which the subspace angles with $\mathbf{V}_{i_0}$ are smaller than $\theta_{\max}$ can be determined and all ROM truncated to the index

$$L = \min_{i=1,\cdots,N_{\mathrm{DB}}} \ell_i. \tag{18}$$

Truncating the ROMs will result in a loss of accuracy of each ROM when compared to the underlying HDM. However, this truncation step will improve accuracy after interpolation of the elements of the database as these will be more consistent.

3.3. Enforcement in the case of arbitrary underlying meshes

In the case of arbitrary meshes, subspace angles cannot be defined as the underlying HDM spaces may be of different, parameter-dependent dimensions $N(\boldsymbol{\mu}_i)$. To address this issue, a heuristic procedure is developed in this section to enforce consistency for that specific scenario. As in the case of the Procrustes problem, one of the ROMs $\mathcal{R}_{i_0}$ is selected to define a reference configuration. Then, for each ROM $\mathcal{R}_i,\ i = 1, \cdots, N_{\text{DB}}$ in the database, a transformed ROM $\mathcal{R}_i^\star$ is determined as the minimizer of a measure of distance of the reference ROM $\mathcal{R}_{i_0}$ to the equivalence class $\mathcal{C}(\mathcal{R}_i)$ as

$$\mathcal{R}_i^\star = \underset{\mathcal{R}\in\mathcal{C}(\mathcal{R}_i)}{\text{argmin}}\ D_{i_0}(\mathcal{R}, \mathcal{R}_{i_0}). \tag{19}$$

The minimization problem is schematically depicted in Fig. 1.

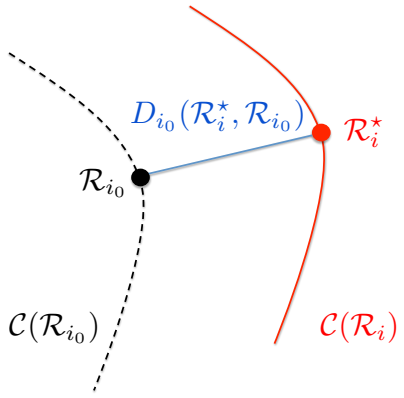

Figure 1 Schematic description of the minimization problem for consistency enforcement in the case of arbitrary meshes

The measure of distance $D_{i_0}(\mathcal{R}, \mathcal{R}_{i_0})$ is defined as follows:

1. For a first-order system, the distance between $\mathcal{R} = (\mathbf{E}_r, \mathbf{A}_r, \mathbf{B}_r, \mathbf{G}_r, \mathbf{H})$ and $\mathcal{R}' = (\mathbf{E}'_r, \mathbf{A}'_r, \mathbf{B}'_r, \mathbf{G}'_r, \mathbf{H}')$ is defined as the normalized expression

$$D_{i_0}(\mathcal{R}, \mathcal{R}') = \epsilon\|\mathbf{E}_r - \mathbf{E}'_r\|_F^2 + \alpha\|\mathbf{A}_r - \mathbf{A}'_r\|_F^2 + \beta\|\mathbf{B}_r - \mathbf{B}'_r\|_F^2 + \gamma\|\mathbf{G}_r - \mathbf{G}'_r\|_F^2 + \eta\|\mathbf{H} - \mathbf{H}'\|_F^2 \tag{20}$$

where

$$\epsilon = \frac{1}{\|\mathbf{E}_r^0\|_F^2},\ \alpha = \frac{1}{\|\mathbf{A}_r^0\|_F^2},\ \beta = \frac{1}{\|\mathbf{B}_r^0\|_F^2},\ \gamma = \frac{1}{\|\mathbf{G}_r^0\|_F^2},\ \eta = \frac{1}{\|\mathbf{H}^0\|_F^2} \tag{21}$$

are normalization constants based on the reduced operators in $\mathcal{R}_{i_0} = (\mathbf{E}_r^0, \mathbf{A}_r^0, \mathbf{B}_r^0, \mathbf{G}_r^0, \mathbf{H}^0)$.

2. For a second-order system, the distance between $\mathcal{R} = (\mathbf{M}_r, \mathbf{C}_r, \mathbf{K}_r, \mathbf{B}_r, \mathbf{G}_r, \mathbf{H})$ and $\mathcal{R}' = (\mathbf{M}'_r, \mathbf{C}'_r, \mathbf{K}'_r, \mathbf{B}'_r, \mathbf{G}'_r, \mathbf{H}')$ is defined as

$$D_{i_0}(\mathcal{R}, \mathcal{R}') = \mu\|\mathbf{M}_r - \mathbf{M}'_r\|_F^2 + \xi\|\mathbf{C}_r - \mathbf{C}'_r\|_F^2 + \kappa\|\mathbf{K}_r - \mathbf{K}'_r\|_F^2 + \beta\|\mathbf{B}_r - \mathbf{B}'_r\|_F^2 + \gamma\|\mathbf{G}_r - \mathbf{G}'_r\|_F^2 + \eta\|\mathbf{H} - \mathbf{H}'\|_F^2 \tag{22}$$

where

$$\mu = \frac{1}{\|\mathbf{M}_r^0\|_F^2},\ \xi = \frac{1}{\|\mathbf{C}_r^0\|_F^2},\ \kappa = \frac{1}{\|\mathbf{K}_r^0\|_F^2} \tag{23}$$

are normalization constants based on the reduced operators in $\mathcal{R}_{i_0} = (\mathbf{M}_r^0, \mathbf{C}_r^0, \mathbf{K}_r^0, \mathbf{B}_r^0, \mathbf{G}_r^0, \mathbf{H}^0)$.

In practice, since the class $\mathcal{C}(\mathcal{R}_i)$ is parameterized by two transformation matrices $\mathbf{Q}$ and $\mathbf{Z}$, the optimization problem (19) can be explicitly written for a first-order system in terms of $\mathcal{R}_i = (\mathbf{E}_{ri}, \mathbf{A}_{ri}, \mathbf{B}_{ri}, \mathbf{G}_{ri}, \mathbf{H}_i)$, $\mathcal{R}_{i_0}$ and $(\mathbf{Q}, \mathbf{Z})$ as

$$\begin{aligned} \min_{\mathbf{Q},\mathbf{Z}} \quad & \epsilon\|\mathbf{Z}^T\mathbf{E}_{ri}\mathbf{Q} - \mathbf{E}_r^0\|_F^2 + \alpha\|\mathbf{Z}^T\mathbf{A}_r\mathbf{Q} - \mathbf{A}_r^0\|_F^2 + \beta\|\mathbf{Z}^T\mathbf{B}_r - \mathbf{B}_r^0\|_F^2 + \gamma\|\mathbf{G}_r\mathbf{Q} - \mathbf{G}_r^0\|_F^2 + \eta\|\mathbf{H} - \mathbf{H}^0\|_F^2 \\ \text{s.t. } & \mathbf{Q}^T\mathbf{Q} = \mathbf{I}_k, \quad \mathbf{Z}^T\mathbf{Z} = \mathbf{I}_k. \end{aligned} \tag{24}$$

A similar expression holds for second-order systems. The rest of this section will focus on first-order systems but the analysis directly carries over to second-order systems as well.

Remark. In the case of Galerkin projection, $\mathbf{W}(\boldsymbol{\mu}_i) = \mathbf{V}(\boldsymbol{\mu}_i)$ and $\mathbf{Q} = \mathbf{Z}$. Then (19) simplifies to

$$\begin{aligned} \min_{\mathbf{Q}} \quad & \epsilon\|\mathbf{Q}^T\mathbf{E}_{ri}\mathbf{Q} - \mathbf{E}_r^0\|_F^2 + \alpha\|\mathbf{Q}^T\mathbf{A}_r\mathbf{Q} - \mathbf{A}_r^0\|_F^2 + \beta\|\mathbf{Q}^T\mathbf{B}_r - \mathbf{B}_r^0\|_F^2 + \gamma\|\mathbf{G}_r\mathbf{Q} - \mathbf{G}_r^0\|_F^2 + \eta\|\mathbf{H} - \mathbf{H}^0\|_F^2 \\ \text{s.t. } & \mathbf{Q}^T\mathbf{Q} = \mathbf{I}_k. \end{aligned} \tag{25}$$

Problem (24) is equivalent to the maximization problem [18]

$$\begin{aligned} \max_{\mathbf{Q},\mathbf{Z}} \quad & \langle \epsilon\mathbf{Z}^T\mathbf{E}_{ri}\mathbf{Q}, \mathbf{E}_r^0\rangle + \langle \alpha\mathbf{Z}^T\mathbf{A}_{ri}\mathbf{Q}, \mathbf{A}_r^0\rangle + \langle \beta\mathbf{B}_r\left(\mathbf{B}_r^0\right)^T, \mathbf{Z}\rangle + \langle \gamma(\mathbf{G}_r^0)^T\mathbf{G}_r, \mathbf{Q}\rangle \\ \text{s.t. } & \mathbf{Q}^T\mathbf{Q} = \mathbf{I}_k, \quad \mathbf{Z}^T\mathbf{Z} = \mathbf{I}_k, \end{aligned} \tag{26}$$

where

$$\langle \mathbf{M}, \mathbf{N}\rangle = \mathrm{tr}(\mathbf{M}^T\mathbf{N}), \quad \mathbf{M}, \mathbf{N} \in \mathbb{R}^{m\times n}. \tag{27}$$

The problem of maximizing the first term in Eq. (26) has been studied in the literature [26, 27] in the case $\mathbf{Q} = \mathbf{Z}$ (Galerkin projection). This first term defines a correlation criterion between the matrices $\mathbf{E}_{ri}$ and $\mathbf{E}_r^0$. A solution to that problem developed in Ref. [26], consists of defining an iterative algorithm whose fixed points are the critical points of the maximization problem. This approach is here extended to the optimization problem of interest for enforcing consistency between ROM operators. Both Galerkin and Petrov-Galerkin projections are considered as follows.

- Galerkin projection.

  In this case, the functional in (26) is

  $$\mathcal{J}_G(\mathbf{Q}) = \langle \epsilon\mathbf{Q}^T\mathbf{E}_{ri}\mathbf{Q}, \mathbf{E}_r^0\rangle + \langle \alpha\mathbf{Q}^T\mathbf{A}_{ri}\mathbf{Q}, \mathbf{A}_r^0\rangle + \langle \beta\mathbf{B}_r\left(\mathbf{B}_r^0\right)^T, \mathbf{Q}\rangle + \langle \gamma(\mathbf{G}_r^0)^T\mathbf{G}_r, \mathbf{Q}\rangle. \tag{28}$$

  Adapting the algorithm developed in [26] to the present case, the iterative algorithm is based on an affine map defined as

  $$\mathbf{M}_{s,\mathrm{G}}(\mathbf{Q}) = \epsilon\left(\mathbf{E}_{ri}\mathbf{Q}\left(\mathbf{E}_r^0\right)^T + \mathbf{E}_{ri}^T\mathbf{Q}\mathbf{E}_r^0\right) + \alpha\left(\mathbf{A}_{ri}\mathbf{Q}\left(\mathbf{A}_r^0\right)^T + \mathbf{A}_{ri}^T\mathbf{Q}\mathbf{A}_r^0\right) + s\mathbf{Q} + \beta\mathbf{B}_{ri}\left(\mathbf{B}_r^0\right)^T + \gamma\mathbf{G}_{ri}^T\mathbf{G}_r^0, \tag{29}$$

  where s is a fixed real parameter chosen such that $s > s_{\min,\mathrm{G}}$ with

  $$s_{\min,\mathrm{G}} = 2\epsilon\left\|\mathbf{E}_{ri}\right\|_2\left\|\mathbf{E}_r^0\right\|_2 + 2\alpha\left\|\mathbf{A}_{ri}\right\|_2\left\|\mathbf{A}_r^0\right\|_2 + \left\|\beta\mathbf{B}_{ri}\left(\mathbf{B}_r^0\right)^T + \gamma\mathbf{G}_{ri}^T\mathbf{G}_r^0\right\|_2. \tag{30}$$

  Defining the parameter s is necessary to ensure that the fixed points of the proposed iterative algorithm are exactly the critical points of the maximization problem (see Theorem 1).

  The proposed procedure then proceeds by iteratively solving the maximization problem

  $$\mathbf{Q}_{j+1} = \arg\max_{\mathbf{S}^T\mathbf{S}=\mathbf{I}_k} \langle \mathbf{S}, \mathbf{M}_{s,\mathrm{G}}(\mathbf{S}_j)\rangle, \quad j = 0, \cdots. \tag{31}$$

The solution to this problem is established in the following lemma, leading to the proposed iterative procedure presented in Algorithm 1.

Lemma. Let the singular value decomposition of $\mathbf{M}_{s,\mathrm{G}}(\mathbf{Q}_j)$ be defined as

$$\mathbf{M}_{s,\mathrm{G}}(\mathbf{Q}_j) = \mathbf{U}\boldsymbol{\Sigma}\mathbf{V}^T. \tag{32}$$

Then

$$\max_{\mathbf{Q}^T\mathbf{Q}=\mathbf{I}_k} \langle \mathbf{Q}, \mathbf{M}_s(\mathbf{Q}_j)\rangle = \sum_{\ell=1}^{k} \sigma_\ell(\mathbf{M}_{s,\mathrm{G}}(\mathbf{Q}_j)), \tag{33}$$

where $\{\sigma_\ell(\mathbf{M}_{s,\mathrm{G}}(\mathbf{Q}_j))\}_{\ell=1}^k$ is the set of singular values of $\mathbf{M}_{s,\mathrm{G}}(\mathbf{Q}_j)$. The solution to the maximization problem is unique and equal to $\mathbf{U}\mathbf{V}^T$.

A proof is offered in [26] in a more general setting.

Algorithm 1 Fixed-point procedure in the case of Galerkin projection

1: Compute $s > 2\epsilon \left\|\mathbf{E}_{ri}\right\|_2 \left\|\mathbf{E}_r^0\right\|_2 + 2\alpha \left\|\mathbf{A}_{ri}\right\|_2 \left\|\mathbf{A}_r^0\right\|_2 + \left\|\beta \mathbf{B}_{ri} \left(\mathbf{B}_r^0\right)^T + \gamma \mathbf{G}_{ri}^T \mathbf{G}_r^0\right\|_2$.

2: Compute $\mathbf{F} = \beta \mathbf{B}_{ri} \left(\mathbf{B}_r^0\right)^T + \gamma \mathbf{G}_{ri}^T \mathbf{G}_r^0$.

3: Choose an orthogonal initial matrix $\mathbf{Q}_0 \in \mathbb{R}^{k\times k}$.

4: **for** $j = 0, \cdots$ **do**

5: Compute the map

$$\mathbf{M}_{s,\mathrm{G}}(\mathbf{Q}_j) = \epsilon \left(\mathbf{E}_{ri}\mathbf{Q}_j \left(\mathbf{E}_r^0\right)^T + \mathbf{E}_{ri}^T\mathbf{Q}_j\mathbf{E}_r^0\right) + \alpha \left(\mathbf{A}_{ri}\mathbf{Q}_j \left(\mathbf{A}_r^0\right)^T + \mathbf{A}_{ri}^T\mathbf{Q}_j\mathbf{A}_r^0\right) + s\mathbf{Q}_j + \mathbf{F}$$

6: Compute its SVD

$$\mathbf{U}_{j+1}\boldsymbol{\Sigma}_{j+1}\mathbf{V}_{j+1}^T = \mathbf{M}_{s,\mathrm{G}}(\mathbf{Q}_j)$$

7: $\mathbf{Q}_{j+1} = \mathbf{U}_{j+1}\mathbf{V}_{j+1}^T$

8: **end for**

In order to show that the fixed points of the recursive algorithm are the critical points of $\mathcal{J}_G$, one needs to characterize these critical points. This is done in the following theorem.

Theorem 1. The critical points $\mathbf{Q}^\star$ of $\mathcal{J}_G$ are orthogonal matrices satisfying the identity

$$\mathbf{Q}^\star\mathbf{S} = \epsilon \left(\mathbf{E}_{ri}\mathbf{Q}^\star \left(\mathbf{E}_r^0\right)^T + \mathbf{E}_{ri}^T\mathbf{Q}^\star\mathbf{E}_r^0\right) + \alpha \left(\mathbf{A}_{ri}\mathbf{Q}^\star \left(\mathbf{A}_r^0\right)^T + \mathbf{A}_{ri}^T\mathbf{Q}^\star\mathbf{A}_r^0\right) + \beta\mathbf{B}_{ri}\left(\mathbf{B}_r^0\right)^T + \gamma\mathbf{G}_{ri}^T\mathbf{G}_r^0, \tag{34}$$

where $\mathbf{S}$ is a symmetric matrix.

A proof is offered in Appendix 1.

Theorem 2. The set of the fixed points of the recursive Algorithm 1 is exactly the set of the critical points of $\mathcal{J}_G$.

A proof of the theorem is presented in Appendix 2.

- Petrov-Galerkin projection.

  Defining the functional

$$\mathcal{J}_{PG}(\mathbf{Q},\mathbf{Z}) = \langle \epsilon\mathbf{Z}^T\mathbf{E}_{ri}\mathbf{Q}, \mathbf{E}_r^0\rangle + \langle \alpha\mathbf{Z}^T\mathbf{A}_{ri}\mathbf{Q}, \mathbf{A}_r^0\rangle + \langle \beta\mathbf{B}_r\left(\mathbf{B}_r^0\right)^T, \mathbf{Z}\rangle + \langle \gamma(\mathbf{G}_r^0)^T\mathbf{G}_r, \mathbf{Q}\rangle, \tag{35}$$

the iterative algorithm is now based on the block-affine map defined as

$$\begin{aligned}\mathbf{M}_{s,\mathrm{PG}}(\mathbf{Q},\mathbf{Z}) &= \begin{bmatrix} \mathbf{M}^{Q}_{s,\mathrm{PG}}(\mathbf{Q},\mathbf{Z}) & \mathbf{0} \\ \mathbf{0} & \mathbf{M}^{Z}_{s,\mathrm{PG}}(\mathbf{Q},\mathbf{Z}) \end{bmatrix} \\ &= \epsilon \begin{bmatrix} \mathbf{0} & \mathbf{E}_{ri} \\ \mathbf{E}_{ri}^T & \mathbf{0} \end{bmatrix} \begin{bmatrix} \mathbf{Q} & \mathbf{0} \\ \mathbf{0} & \mathbf{Z} \end{bmatrix} \begin{bmatrix} \mathbf{0} & \left(\mathbf{E}_r^0\right)^T \\ \left(\mathbf{E}_r^0\right)^T & \mathbf{0} \end{bmatrix} \\ &\quad + \alpha \begin{bmatrix} \mathbf{0} & \mathbf{A}_{ri} \\ \mathbf{A}_{ri}^T & \mathbf{0} \end{bmatrix} \begin{bmatrix} \mathbf{Q} & \mathbf{0} \\ \mathbf{0} & \mathbf{Z} \end{bmatrix} \begin{bmatrix} \mathbf{0} & \left(\mathbf{A}_r^0\right)^T \\ \left(\mathbf{A}_r^0\right)^T & \mathbf{0} \end{bmatrix} \\ &\quad + s \begin{bmatrix} \mathbf{Q} & \mathbf{0} \\ \mathbf{0} & \mathbf{Z} \end{bmatrix} + \begin{bmatrix} \beta \mathbf{B}_{ri} \left(\mathbf{B}_r^0\right)^T & \mathbf{0} \\ \mathbf{0} & \gamma \mathbf{G}_{ri}^T \mathbf{G}_r^0 \end{bmatrix},\end{aligned} \tag{36}$$

where s is chosen such that $s > s_{\min,\mathrm{PG}}$ with

$$s_{\min,\mathrm{PG}} = \epsilon \left\|\mathbf{E}_{ri}\right\|_2 \left\|\mathbf{E}_r^0\right\|_2 + \alpha \left\|\mathbf{A}_{ri}\right\|_2 \left\|\mathbf{A}_r^0\right\|_2 + \max\left(\beta \left\|\mathbf{B}_{ri}\left(\mathbf{B}_r^0\right)^T\right\|_2, \gamma \|\mathbf{G}_{ri}^T \mathbf{G}_r^0\|_2\right). \tag{37}$$

Similarly as in the case of Galerkin projection, a fixed point procedure is defined in Algorithm 2. The

Algorithm 2 Fixed-point procedure in the case of Petrov-Galerkin projection

1: Compute $s > \epsilon \left\|\mathbf{E}_{ri}\right\|_2 \left\|\mathbf{E}_r^0\right\|_2 + \alpha \left\|\mathbf{A}_{ri}\right\|_2 \left\|\mathbf{A}_r^0\right\|_2 + \max\left(\beta \left\|\mathbf{B}_{ri}\left(\mathbf{B}_r^0\right)^T\right\|_2, \gamma \|\mathbf{G}_{ri}^T \mathbf{G}_r^0\|_2\right)$.
2: Compute $\mathbf{F}_B = \beta \mathbf{B}_{ri}\left(\mathbf{B}_r^0\right)^T$ and $\mathbf{F}_G = \gamma \mathbf{G}_{ri}^T \mathbf{G}_r^0$.
3: Choose orthogonal initial matrices $\mathbf{Q}_0 \in \mathbb{R}^{k\times k}$ and $\mathbf{Z}_0 \in \mathbb{R}^{k\times k}$.
4: **for** $j = 0, \cdots$ **do**
5: Compute the maps

$$\mathbf{M}^{Q}_{s,\mathrm{PG}}(\mathbf{Q}_j,\mathbf{Z}_j) = \epsilon \mathbf{E}_{ri}\mathbf{Z}_j\left(\mathbf{E}_r^0\right)^T + \alpha \mathbf{A}_{ri}\mathbf{Z}_j\left(\mathbf{A}_r^0\right)^T + s\mathbf{Q}_j + \mathbf{F}_G$$

and

$$\mathbf{M}^{Z}_{s,\mathrm{PG}}(\mathbf{Q}_j,\mathbf{Z}_j) = \epsilon \mathbf{E}_{ri}^T\mathbf{Q}_j\left(\mathbf{E}_r^0\right)^T + \alpha \mathbf{A}_{ri}^T\mathbf{Q}_j\left(\mathbf{A}_r^0\right)^T + s\mathbf{Z}_j + \mathbf{F}_B$$

6: Compute their SVDs

$$\mathbf{U}^{Q}_{j+1}\mathbf{\Sigma}^{Q}_{j+1}\mathbf{V}^{QT}_{j+1} = \mathbf{M}^{Q}_{s,\mathrm{PG}}(\mathbf{Q}_j)$$

and

$$\mathbf{U}^{Z}_{j+1}\mathbf{\Sigma}^{Z}_{j+1}\mathbf{V}^{ZT}_{j+1} = \mathbf{M}^{Z}_{s,\mathrm{PG}}(\mathbf{Q}_j)$$

7: $\mathbf{Q}_{j+1} = \mathbf{U}^{Q}_{j+1}\mathbf{V}^{QT}_{j+1}$
8: $\mathbf{Z}_{j+1} = \mathbf{U}^{Z}_{j+1}\mathbf{V}^{ZT}_{j+1}$
9: **end for**

following theorems, whose proofs follow closely the ones of Theorems 1 and 2, establish the fact that the fixed point procedure in Algorithm 2 can be used to find critical points of $\mathcal{J}_{PG}$.

Theorem 3 The critical points $(\mathbf{Q}^\star, \mathbf{Z}^\star)$ of $\mathcal{J}_{PG}$ are orthogonal matrices satisfying the identities

$$\begin{aligned}\mathbf{Q}^\star\mathbf{S}_Q &= \epsilon \mathbf{E}_{ri}\mathbf{Z}^\star\left(\mathbf{E}_r^0\right)^T + \alpha \mathbf{A}_{ri}\mathbf{Z}^\star\left(\mathbf{A}_r^0\right)^T + \gamma \mathbf{G}_{ri}^T\mathbf{G}_r^0, \\ \mathbf{Z}^\star\mathbf{S}_Z &= \epsilon \mathbf{E}_{ri}^T\mathbf{Q}^\star\left(\mathbf{E}_r^0\right)^T + \alpha \mathbf{A}_{ri}^T\mathbf{Q}^\star\left(\mathbf{A}_r^0\right)^T + \beta \mathbf{B}_{ri}\left(\mathbf{B}_r^0\right)^T,\end{aligned} \tag{38}$$

where $\mathbf{S}_Q$ and $\mathbf{S}_Z$ are symmetric matrices.

Theorem 4. The set of the fixed points of the recursive Algorithm 2 is exactly the set of the critical points of $\mathcal{J}_{PG}$.

Remark. For the case of arbitrary meshes, assessing consistency is a more difficult task as two conflicting factors intervene in the distance measure D_{i_0}: (1) the inconsistency arising from a choice of two distinct sets of coordinates and (2) the inherent variation of the ROM operators due to parameter changes.

3.4. Consistent set of reduced-order models

After the computation of the optimal transformation operators $\{(\mathbf{Z}^\star(\boldsymbol{\mu}_i), \mathbf{Q}^\star(\boldsymbol{\mu}_i))\}_{i=1}^{N_\mu}$, the reduced operators in the database $\mathcal{DB}$ are transformed accordingly as

$$\begin{aligned}\mathcal{DB} &= \{\boldsymbol{\mu}_i; (\mathbf{E}_r^\star(\boldsymbol{\mu}_i), \mathbf{A}_r^\star(\boldsymbol{\mu}_i), \mathbf{B}_r^\star(\boldsymbol{\mu}_i), \mathbf{G}_r^\star(\boldsymbol{\mu}_i), \mathbf{H}_r^\star(\boldsymbol{\mu}_i))\}_{i=1}^{N_\mu} \\ &= \left\{\boldsymbol{\mu}_i; \left(\mathbf{Z}^\star(\boldsymbol{\mu}_i)^T\mathbf{E}_r(\boldsymbol{\mu}_i)\mathbf{Q}^\star(\boldsymbol{\mu}_i), \mathbf{Z}^\star(\boldsymbol{\mu}_i)^T\mathbf{A}_r(\boldsymbol{\mu}_i)\mathbf{Q}^\star(\boldsymbol{\mu}_i), \mathbf{Z}^\star(\boldsymbol{\mu}_i)^T\mathbf{B}_r(\boldsymbol{\mu}_i), \mathbf{G}_r^\star(\boldsymbol{\mu}_i)\mathbf{Q}^\star(\boldsymbol{\mu}_i), \mathbf{H}_r(\boldsymbol{\mu}_i)\right)\right\}_{i=1}^{N_\mu}.\end{aligned} \tag{39}$$

Similar expressions hold for the case of second-order systems.

4. Interpolation in a database of ROMs on matrix manifolds

4.1. Interpolation

As indicated in Section 2, the interpolation of the linear operators stored in the database $\mathcal{DB}$ should often preserve properties of the operators such as symmetry, positivity, orthogonality or non-singularity. An approach to preserve these properties was first presented in [10]. It is based on the interpolation on the tangent space of the appropriate manifold and was applied to the case of interpolation of reduced operators in [17, 19, 21].

The algorithm proceeds for each of the elements of the database in four steps as follows:

1. An identification of the manifold the reduced matrices belong to
2. A mapping (logarithmic map) of all the database reduced matrices to the tangent space of the manifold at one of the database points
3. An interpolation of the mapped quantities in the tangent space at the target parameter $\boldsymbol{\mu}$
4. A mapping (exponential map) of the interpolated quantity back to the manifold leading to a reduced operator at the target parameter $\boldsymbol{\mu}$

More details on the interpolation algorithm as well as the formulas for computing the mapping are provided in [21, 18].

In practice there may be several choices for an interpolation procedure on matrix manifolds as underlined by the following two cases.

- In [19], the authors develop a heuristic technique for interpolating non-singular matrices either on the manifold on non-singular matrices or square matrices. The heuristic proceeds by selecting the manifold for which a nonlinearity criterion is the smallest. This heuristic is applied in Section 5.2.
- An alternative to interpolating symmetric positive definite matrices on the tangent space to that manifold is to use the Choleski factorization. This novel approach is described in Algorithm 3 and applied in Section 5.1. This approach avoids selecting one of the database points and interpolating in its associated tangent space. It preserves the SPD properties of the matrices as long as the interpolated quantity on the diagonal of the Choleski factor are all strictly non zero.

There is no restriction on the interpolation technique in the tangent space to the matrix manifold of interest as long as the it leads to an interpolated quantity that preserves the tangent space [21]. In [28], the author identifies an interpolation technique that does not preserve that property. When the database parameters belong to a lattice of points, spline or polynomial interpolation can be used in the tangent space. When the dimension $N_{\boldsymbol{\mu}}$ of the parameter domain is large, however, interpolating from a lattice of points is not an option and instead, interpolation based on radial basis functions or Kriging can be used instead [10, 18, 29].

Algorithm 3 Interpolation of SPD matrices by Choleski factorization

1: **for** $i = 1, \cdots, N_{\text{DB}}$ **do**
2: Compute the Choleski factorization

$$\mathbf{K}_{ri} = \mathbf{S}_i \mathbf{S}_i^T$$

3: **end for**
4: Interpolate the Choleski factors $\{\mathbf{S}_i\}_{i=1}^{N_{\text{DB}}}$, leading to an interpolated factor $\mathbf{S}^\star$
5: Compute the interpolated matrix as

$$\mathbf{K}_r^\star = \mathbf{S}^\star \mathbf{S}^{\star T}$$

4.2. Sampling

The selection of sample points $\{\boldsymbol{\mu}_i\}_{i=1}^{N_{DB}}$ is an important step that influences the accuracy of the resulting interpolation approach. A poor choice of sample points will result in large errors of the proposed procedure in some regions of the parameter domain $\mathcal{D}$. A priori sampling techniques such as factorial and latin hypercube sampling can be used to provide a uniform coverage of $\mathcal{D}$. Alternatively, greedy techniques that iteratively sample the regions of the parameter space associated with the largest ROM error can provide a selection of the samples that is more suited for the problem of interest. Such greedy techniques have been introduced in the context of model reduction in general in [9, 30, 31, 13, 14, 32] and for interpolation of LTIP ROM systems in particular in [29]. A priori sampling will be used in the application of Section 5.2 and a greedy sampling approach developed for the inverse problem application of Section 5.1.

4.3. Storage and exploitation

In practice the reduced operators are stored after their congruence transformation in one database $\mathcal{DB}$ or several sub-databases $\{\mathcal{DB}_f\}_{s=1}^{N_s}$ of the form

$$\mathcal{DB} = \bigcup_{s=1}^{N_S} \mathcal{DB}_s = \bigcup_{s=1}^{N_S} \{\boldsymbol{\mu}_i; (\mathbf{E}_r^\star(\boldsymbol{\mu}_i), \mathbf{A}_r^\star(\boldsymbol{\mu}_i), \mathbf{B}_r^\star(\boldsymbol{\mu}_i), \mathbf{G}_r^\star(\boldsymbol{\mu}_i), \mathbf{H}^\star(\boldsymbol{\mu}_i))\}_{i=1}^{N_{DB,s}} \tag{40}$$

for first-order systems and

$$\mathcal{DB} = \bigcup_{s=1}^{N_S} \mathcal{DB}_s = \bigcup_{s=1}^{N_S} \{\boldsymbol{\mu}_i; (\mathbf{M}_r^\star(\boldsymbol{\mu}_i), \mathbf{C}_r^\star(\boldsymbol{\mu}_i), \mathbf{K}_r^\star(\boldsymbol{\mu}_i), \mathbf{B}_r^\star(\boldsymbol{\mu}_i), \mathbf{G}_r^\star(\boldsymbol{\mu}_i), \mathbf{H}^\star(\boldsymbol{\mu}_i))\}_{i=1}^{N_{DB,s}} \tag{41}$$

for second-order systems.

Storing the database is inexpensive as it only involves reduced operators. In practice, a database with $N_{DB} = \sum_{s=1}^{S} N_{DB,s}$ contains $N_{DB}(N_{\boldsymbol{\mu}} + 2k^2 + k(N_i + N_o) + N_i N_o)$ matrix entries for first-order systems of the form (1) and $N_{DB}(N_{\boldsymbol{\mu}} + 3k^2 + k(N_i + N_o) + N_i N_o)$ entries for second-order systems of the form (4).

The parameter domain $\mathcal{D}$ is in practice subdivided in N_S non-overlaping subdomains $\{\mathcal{D}_s\}_{s=1}^{N_S}$ such that

$$\mathcal{D} = \bigcup_{s=1}^{N_S} \mathcal{D}_s \tag{42}$$

and each subdomain $\mathcal{D}_s$ is associated with the sub-database $\mathcal{DB}_s$. Then, in the online phase, for a new value $\widehat{\boldsymbol{\mu}} \in \mathcal{D}$ of the parameters, the sub-database $\mathcal{DB}_{s_0}$ it belongs to is readily identified and reduced-operators computed for $\widehat{\boldsymbol{\mu}}$ using the ROMs stored in $\mathcal{DB}_{s_0}$.

5. Applications and performance assessment

The proposed approaches are here applied to two challenging physical applications: the acoustic inverse obstacle problem and the aeroelastic flutter problem.

5.1. Acoustic scattering analysis

The acoustic inverse obstacle problem considered here consists in determining the shape of an obstacle or a part of this shape from the knowledge of some scattered far-field patterns, assuming certain characteristics of the surface of the obstacle. It is well-known [33] that such an inverse problem is non-linear and often quite ill-posed, making its numerical solution challenging.

To illustrate the ROM database framework proposed above, a parameter identification problem is considered, where the shape of the obstacle is assumed to be known a-priori, but the vector of parameters $\boldsymbol{\mu} \in \mathbb{R}^{N_\mu}$ of the shape needs to be identified from the measured far-field pattern. This class of problems is a subset of a general acoustic inverse obstacle problem.

In order to describe the considered problem more accurately, the corresponding direct acoustic scattering problem is recalled first. The scattering of time-harmonic acoustic waves by an impenetrable obstacle with the boundary Σ embedded in an infinite homogeneous fluid medium $\Omega_e \subset \mathbb{R}^d$ can be formulated as the following exterior boundary value problem for the unknown acoustic pressure field w in the fluid

$$\begin{aligned} \Delta w + \kappa^2 w &= 0 \quad \text{in} \quad \Omega_e, \\ \left(a + b\frac{\partial}{\partial \boldsymbol{\nu}}\right)\left(w + w^{inc}\right) &= 0 \quad \text{on} \quad \Sigma, \\ \lim_{r\to\infty} r^{\frac{d-1}{2}}\left(\frac{\partial w}{\partial r} - j\kappa w\right) &= 0, \end{aligned} \tag{43}$$

where the incident wave is given by

$$w^{inc} = e^{j\kappa \mathbf{d}\cdot\mathbf{x}},$$

the unit vector $\mathbf{d}$ indicates the direction of the incident plane wave, and either $a \neq 0$ or $b \neq 0$. Sound-hard, sound-soft, or impedance boundary conditions can all be represented by the second equation of (43). In the example below, the sound-hard scattering problem is used, leading to the choice of the Neumann boundary condition ($a = 0$ and $b = 1$). The third equation in (43) is the Sommerfeld radiation condition. It ensures, in the physical sense, that all waves are outgoing and, mathematically, that the direct scattering problem is well-posed for any wavenumber $\kappa = \omega/c$, where ω is the angular frequency of the harmonic oscillations and c is the speed of sound in the fluid.

In order to discretize the direct scattering problem (43), the finite element method is considered. The infinite domain is first truncated, and a perfectly matched layer [34] near the exterior boundary is used to simulate the effect of the Sommerfeld condition. This converts the boundary value problem (43) into that of solving the algebraic system of linear equations

$$\left(\mathbf{K}(\boldsymbol{\mu}) - \kappa^2 \mathbf{M}(\boldsymbol{\mu})\right)\mathbf{w}(\kappa, \boldsymbol{\mu}) = \mathbf{f}(\kappa, \boldsymbol{\mu}) \tag{44}$$

for the unknown degrees of freedom $\mathbf{w} \in \mathbb{C}^N$. This system is a second-order LTI system of the form (5). Here, $\mathbf{K}$ corresponds to the finite element discretization of the Laplace operator, and $\mathbf{M}$ is a mass-type matrix. For an interior problem associated with the Helmholtz equation, $\mathbf{M}$ is real, symmetric positive-definite, and $\mathbf{K}$ is real, symmetric non-negative. When the perfectly matched layer is used, the matrices $\mathbf{K}$ and $\mathbf{M}$ become complex and non-Hermitian. The source vector $\mathbf{f}$ arises from the discretization of the sound-hard boundary condition.

The far field pattern characterizes the asymptotic behavior of the acoustic scattered field far away from the obstacle. In two dimensions, it admits the following integral representation [33]

$$w_\infty(\hat{\mathbf{x}}) \;=\; \frac{e^{j\frac{\pi}{4}}}{(8\pi\kappa)^{\frac{1}{2}}}\int_\Gamma \left(\frac{\partial w}{\partial \boldsymbol{\nu}}(\mathbf{y}) + j\kappa\ \hat{\mathbf{x}}.\boldsymbol{\nu}\ w(\mathbf{y})\right) e^{-j\kappa\hat{\mathbf{x}}.\mathbf{y}} d\sigma_y\ ; \qquad \hat{\mathbf{x}} \in S^1, \tag{45}$$

where S^1 is the unit circle. After computing the finite-element solution, the integral (45) can be evaluated by integrating over a suitable curve Γ (often the boundary Σ) in the computational domain. The integral in (45) evaluated at N_o locations $\hat{x}_1, \cdots, \hat{x}_{N_o}$ of the circle S^1 can then be in practice represented by the action

of a matrix on the solution vector $\mathbf{y}(\kappa,\boldsymbol{\mu}) = \mathbf{G}(\kappa,\boldsymbol{\mu})\mathbf{w}(\kappa,\boldsymbol{\mu})$ with $\mathbf{G} \in \mathbb{C}^{N_o \times N}$. Practically, the following logarithmic scale quantity is usually plotted

$$\mathcal{S}(\hat{\mathbf{x}}) = 10\log_{10}(2\pi|w_\infty(\hat{\mathbf{x}})|^2).$$

This quantity can also be computed for each entry of the output vector $\mathbf{y}(\kappa,\boldsymbol{\mu})$ as

$$\mathbf{s}(\kappa,\boldsymbol{\mu}) = \mathbf{s}\left(\mathbf{y}(\kappa,\boldsymbol{\mu})\right). \tag{46}$$

The inverse problem considered here consists of identifying parameters $\boldsymbol{\mu} = (L^s, t^s) \in \mathcal{D} \subset \mathbb{R}^2$ of a two-dimensional mockup submarine, characterized by its length L^s, and the position of its tower t^s from given far-field data for several frequencies (wavenumbers) $\{\mathbf{s}_m(\kappa_i)\}_{i=1}^{N_\kappa}$. The inverse problem can be written as

$$\begin{aligned} \min_{\boldsymbol{\mu}\in\mathcal{D}} & \sum_{i=1}^{N_\kappa} \alpha_i \left\|\mathbf{s}\left(\mathbf{y}(\kappa_i,\boldsymbol{\mu})\right) - \mathbf{s}_m(\kappa_i)\right\|_2^2 + \frac{\beta}{2}\|\boldsymbol{\mu}\|_2^2 \\ \text{s.t.} \quad & \left(\mathbf{K}(\boldsymbol{\mu}) - \kappa_i^2\mathbf{M}(\boldsymbol{\mu})\right)\mathbf{w}(\kappa_i,\boldsymbol{\mu}) = \mathbf{f}(\kappa_i,\boldsymbol{\mu}), \\ & \mathbf{y}(\kappa_i,\boldsymbol{\mu}) = \mathbf{G}(\kappa_i,\boldsymbol{\mu})\mathbf{w}(\kappa_i,\boldsymbol{\mu}), \quad i = 1,\cdots,N_\kappa, \end{aligned} \tag{47}$$

where a Tikhonov regularization term has been added and $\{\alpha_i\}_{i=1}^{N_\kappa}, \beta$ are appropriate positive weights.

Since the solution of the discrete direct problem (44) for each different wavenumber requires a costly re-factorization of the matrix on the left-hand side, to enable the efficient computations for many wavenumbers, a reduced-order model is built using a derivative-based Galerkin projection (DGP) framework [24] for a given value $\boldsymbol{\mu}$ of the shape parameters. In this method, based on moment-matching, $N_\partial^{\mathrm{DGP}}$ derivatives of the solution with respect to the wavenumber κ are first computed by solving (44) with recursively constructed right-hand sides at N_κ^{DGP} interpolating wavenumbers. Then, these derivatives are orthogonalized to achieve numerical robustness, and used to form a subspace of dimension $k = N_\kappa^{\mathrm{DGP}} N_\partial^{\mathrm{DGP}}$ for Galerkin projection, leading to reduced matrices $\mathbf{K}_r(\boldsymbol{\mu})$, $\mathbf{M}_r(\boldsymbol{\mu})$, $\mathbf{f}_r(\kappa,\boldsymbol{\mu})$ and $\mathbf{G}_r(\kappa,\boldsymbol{\mu})$.

Figure 2 depicts the triangulated computational domain (left) with the elements in the PML layer shown in cyan; the real part of the solution for $\kappa = 20$, $L^s = 1$, and $t^s = 0.2$ is shown on the right. For different values of the shape parameters, the computational domain is remeshed. Isoparametric cubic Finite Elements are used. All computations are done using Matlab.

The solution procedure described in detail below builds a database of frequency-sweep ROMs offline by sampling the shape parameter space adaptively to ensure accuracy. The database of the ROMs is then used to efficiently solve the reduced inverse problem. For a given value of the parameters, $N_\partial^{\mathrm{DGP}} = 8$ (including the 0-th derivative) are computed for the $N_\kappa^{\mathrm{DGP}} = 2$ frequencies $\kappa \in \{10, 20\}$, leading to a ROM of dimension $k = 16$. In the present case, there are $N_0 = 360$ outputs equidistributed on the sphere S^1.

In a first set of numerical experiments, the effect of consistency on predictions based on a database of ROMs is illustrated. For that purpose, a small database of $N_{\mathrm{DB}} = 4$ ROMs is first created for the values of the parameters indicated in Table 1 where the number of dofs for each underlying HDM is also reported. One can observe that each HDM has a different number of dofs.

The consistency enforcement procedure for arbitrary meshes developed in Section 3.3 is first applied to transform the reduced operators prior to their interpolation. In a second case, the operators are not transformed. In all cases, the reduced operators are interpolated on their appropriate manifold at $\boldsymbol{\mu}^\star = [0.9625, 0.1125]$ by bilinear interpolation as follows:

- The operators $\mathrm{Re}(\mathbf{M}_r(\cdot))$, $\mathrm{Im}(\mathbf{M}_r(\cdot))$ and $\mathrm{Re}(\mathbf{K}_r(\cdot))$ are SPD matrices and as such as interpolated on their appropriate manifold using the Choleski decomposition-based approach proposed in Section 4.1.
- The operator $\mathrm{Im}(\mathbf{K}_r(\cdot))$ is interpolated on the manifold of symmetric matrices.
- The operators $\{\mathbf{f}_r(\kappa_i,\cdot), \mathbf{G}_r(\kappa_i,\cdot)\}_{i=1}^{N_\kappa}$ are interpolated on the manifold of rectangular complex matrices.

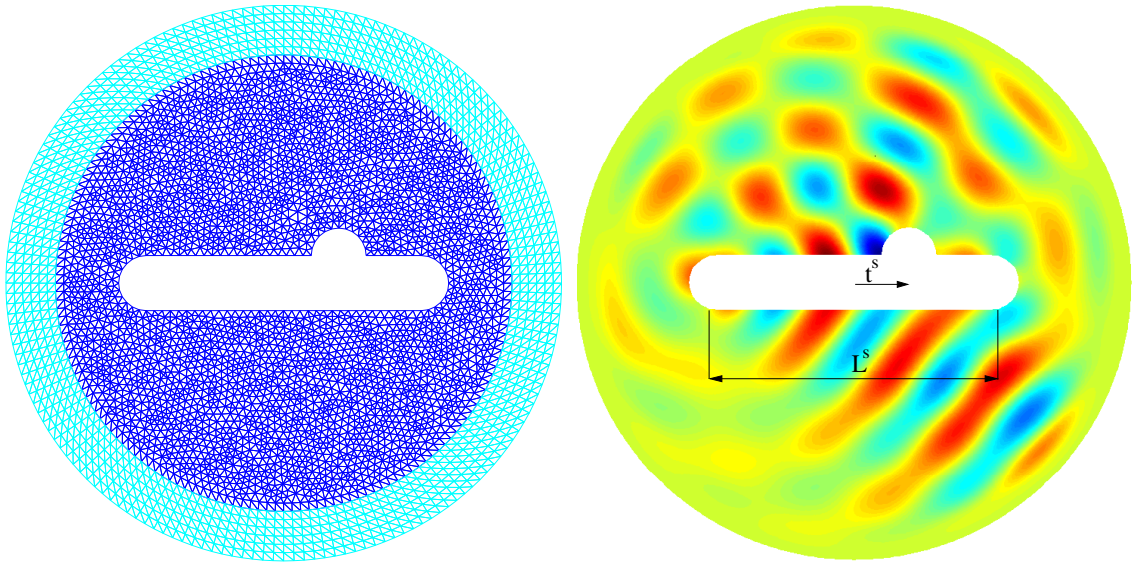

Figure 2 Computational mesh and the real part of the solution for $\kappa = 20$

$\mathcal{DB}$ point	μ_1	μ_2	$N(\boldsymbol{\mu})$
1	0.95	0.1	41,235
2	0.975	0.1	40,965
3	0.95	0.125	41,424
4	0.975	0.125	40,929

Table 1 Database of ROMs and associated underlying HDM number of dofs

Figure 3 reports the far-field pattern for $\kappa = 14$ at $\boldsymbol{\mu}^\star = [0.9625, 0.1125]$ computed by the HDM and the two ROM interpolation approaches. One can observe the importance of consistency as the inconsistent ROM database leads to poor predictions whereas the consistent ROM database predictions very closely follow the HDM results.

Next an adaptive approach for constructing the ROM database is developed. The approach proceeds by comparing the predictions associated with the ROM database and HDM at the center of each hypercube of the database and refining that hypercube if the error is above a given threshold. The error can be associated with an output of interest, such as the far-field pattern, leading to a goal-oriented approach. In the following, the error will be based on the accuracy of the shape $\widehat{\boldsymbol{\mu}}$ returned by solving the reduced inverse problem by simulated annealing.

$$\begin{aligned} &\min_{\boldsymbol{\mu}\in\mathcal{D}} \sum_{i=1}^{N_\kappa} \alpha_i \left\| \mathbf{s}\left(\mathbf{y}_r(\kappa_i,\boldsymbol{\mu})\right) - \mathbf{s}_m(\kappa_i)\right\|_2^2 + \frac{\beta}{2}\|\boldsymbol{\mu}\|_2^2 \\ &\text{s.t.} \quad \left(\mathbf{K}_r(\boldsymbol{\mu}) - \kappa_i^2 \mathbf{M}_r(\boldsymbol{\mu})\right)\mathbf{q}(\kappa_i,\boldsymbol{\mu}) = \mathbf{f}_r(\kappa_i,\boldsymbol{\mu}), \\ &\qquad \mathbf{y}_r(\kappa_i,\boldsymbol{\mu}) = \mathbf{G}_r(\kappa_i,\boldsymbol{\mu})\mathbf{q}(\kappa_i,\boldsymbol{\mu}), \quad i = 1,\cdots,N_\kappa. \end{aligned} \tag{48}$$

The error measure is then defined as

$$\text{Error} = \left\| \frac{\widehat{\boldsymbol{\mu}} - \boldsymbol{\mu}^\star}{\boldsymbol{\mu}_{\max} - \boldsymbol{\mu}_{\min}} \right\|_\infty \tag{49}$$

where $\boldsymbol{\mu}^\star$ denotes the target shapes, $\boldsymbol{\mu}_{\min}$ and $\boldsymbol{\mu}_{\max}$ the lower and upper bounds for each shape parameters, respectively and the ratio in Error is computed entry-by-entry.

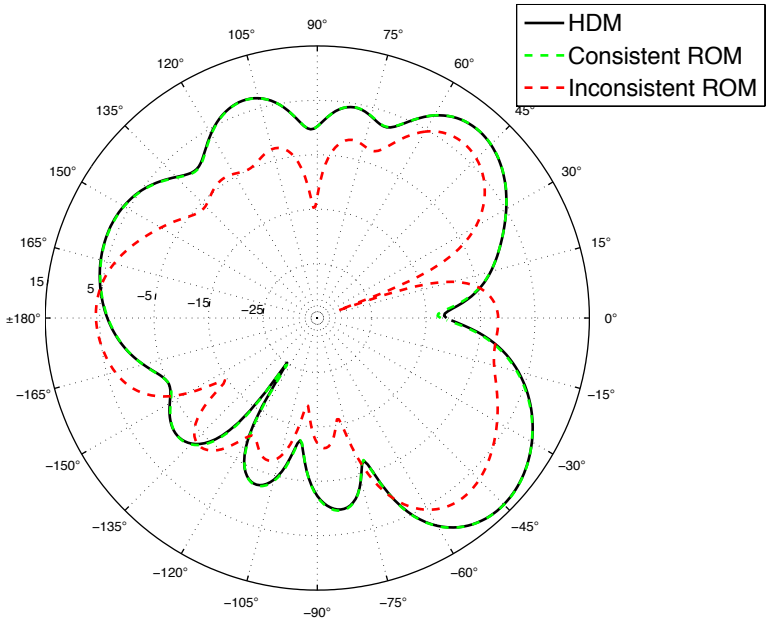

Figure 3 Comparison of the far-field pattern predictions obtained by interpolation of inconsistent and consistent databases.

Figure 4 reports the refined database for an error tolerance of 5% and the parameter domain $\mathcal{D} = [0.9, 1] \times [0.1, 0.2]$. $N_{\text{DB}} = 21$ points are sampled in the domain. The training errors obtained at each iteration refinement of the procedure are reported in Figure 5. One can observe that after the second refinement, all errors are below the error threshold of 5%.

To validate the accuracy of the ROM database, 289 target shape parameters are selected in $\mathcal{D}$ and the reduced inverse problems solved for each of them. The distribution of corresponding errors are reported in Figures 6 and 7. One can observe that all errors are below the error threshold, confirming the validity of the training procedure.

Finally, the CPU timings associated with the solution of a given inverse problem are compared for the HDM and ROM database strategy. The CPU timings are reported in Table 2. One can observe that an impressive speedup of 270 is obtained thanks to the database strategy. For a given function call in the optimization problem, the speedup is equal to 207.

Approach	Error	Number of function calls	Online optimization Wall time	Speedup
HDM	8×10^{-4}	1530	1 h 30 min	1
ROM database	0.02	1176	20.1 s	270

Table 2 Wall times associated with the solution of the inverse problem with the HDM and database of ROMs

5.2. Flutter analysis

The aeroelastic analysis of a wing-store configuration flying in the subsonic, transonic and supersonic regimes is considered. Some properties of that system were originally studied in [35, 36]. Among those, the hydroelastic effects inside the fuel tank modify the structural properties of the wing-store configuration, thereby affecting the flutter characteristic of the system. This justifies parameterizing the aeroelastic system

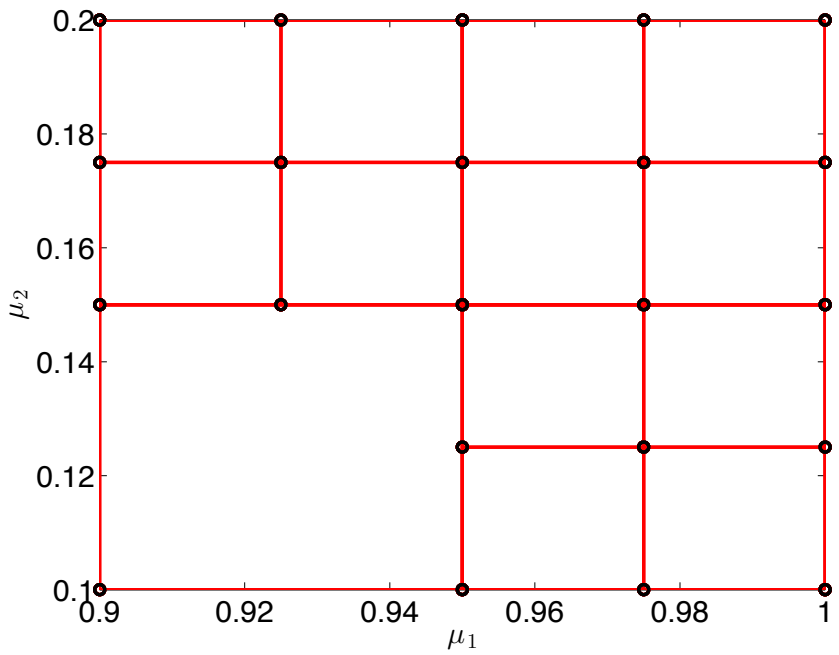

Figure 4 Pre-computed database $\mathcal{DB}$ of reduced-order models selected by the adaptive sampling procedure.

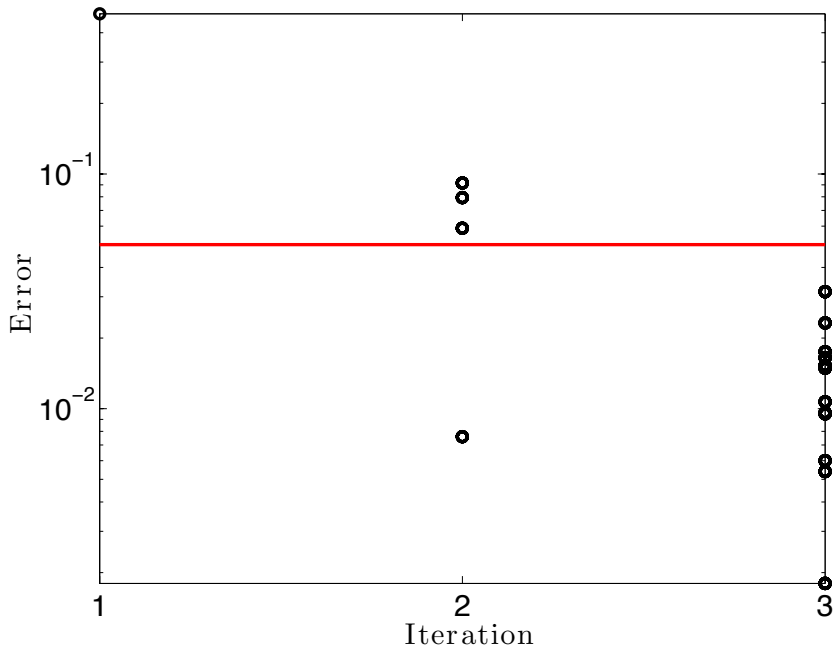

Figure 5 Training errors at each iteration of the adaptive sampling procedure.

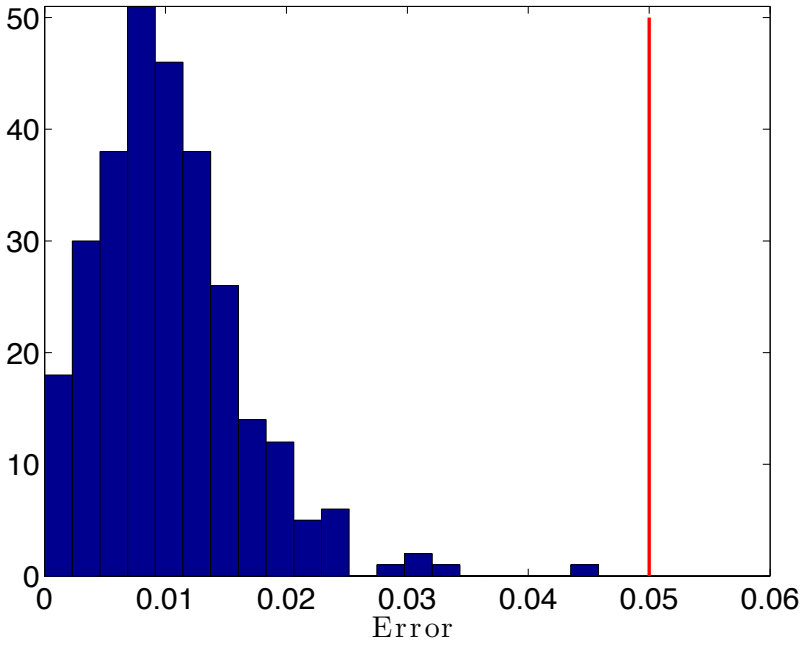

Figure 6 Distribution of prediction errors for the solution of 289 inverse problems.

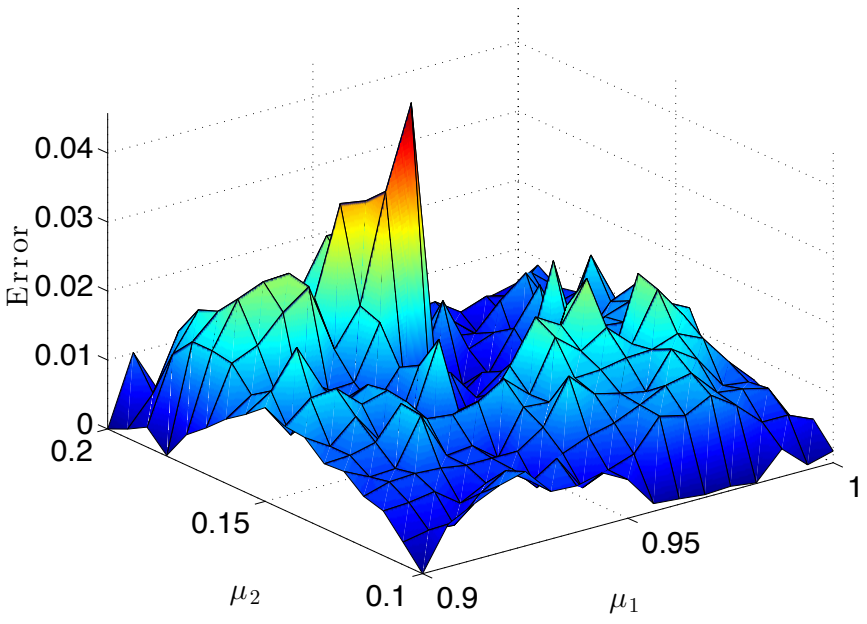

Figure 7 Prediction errors for the solution of 289 inverse problems.

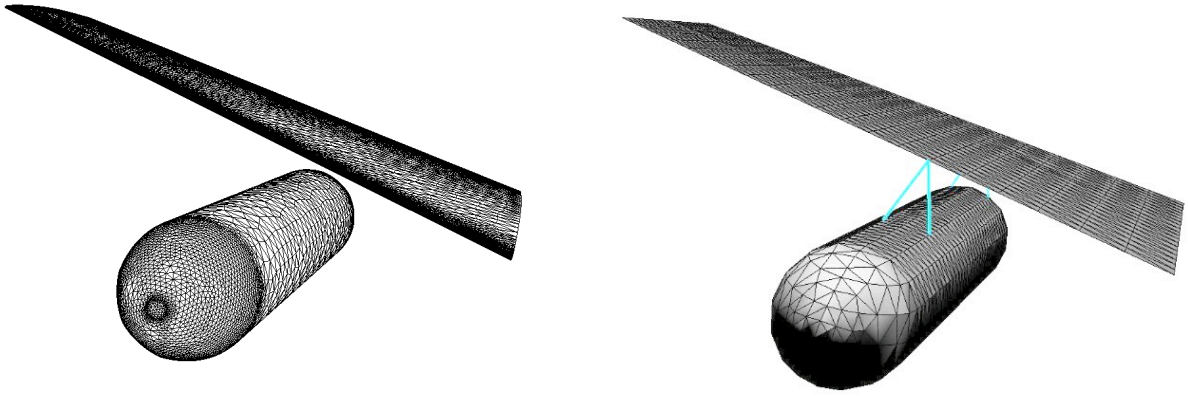

(a) CFD surface grid

(b) FE structural model

Figure 8 High-dimensional aeroelastic model of a wing-store configuration.

by the fuel fill level f inside the tank. Furthermore, the aeroelastic properties of the wing-store system depend heavily on the aerodynamic properties of the configuration. As a result, the system will also be parameterized by the free-stream Mach number M_∞.

The structural and fluid surface models of the wing-store system are graphically depicted in Figure 8. The structural subsystem is a second-order LTIP of the form (4) and is modeled by the Finite Element method. For each fill level, a new structural mesh is generated inside the tank for the full physical domain. The hydroelastic effects are modeled by an added mass effect [35, 36], resulting in a linear HDM with $N^{(s)} = 6,834$ dofs for all values of f. The proposed ROM database approach will enable by-passing the re-meshing of the fuel domain everytime the fill level is varied.

The fluid subsystem is modeled by the linearized Euler equations and discretized by the Finite Volume method using a second-order accurate linear flux reconstruction and a second-order accurate implicit backward difference time integration scheme. For each operating point $\boldsymbol{\mu} = (M_\infty, f)$, the nonlinear fluid HDM is linearized around a steady-state, resulting in a first-order LTIP system of the form (1) with $N^{(f)} \approx 400,000$ dofs.

In this work, the operation domain of interest is $(M_\infty, f) \in \mathcal{D} = [0.6, 1.1] \times [0, 100]$. For each operating point, the critical values of pressure p_∞^{cr} and velocity V_∞^{cr} at the onset of flutter are sought. Once, these quantities are determined, the flutter speed index (FSI) can be computed as

$$\text{FSI} = \frac{V_\infty^{\text{cr}}}{b_s \omega_\alpha \sqrt{\bar{\mu}}}, \tag{50}$$

where b_s is the semi-chord of the wing at its root, ω_α is the first dry torsional mode of the wing-store structural system and $\bar{\mu}$ is the mass ratio as defined in [37, 35, 36].

The flutter speed indices of the system of interest are computed using the HDM for 26 different free-stream Mach number and 5 different fill levels in the domain $(M_\infty, f) \in \mathcal{D}$, resulting in 130 operating points, and reported in Figure 9. One can observe the characteristic flutter dip for $M_\infty \approx 0.96$.

The framework developed in this paper is then applied to the problem of interest to interpolate reduced aeroelastic operators. In this example, all structural and fluid HDMs are defined on the same mesh and the approach of enforcing ROM consistency developed in Section 3.2 is followed. For that purpose, $N_{\text{DB}} = 21$ operating points are sampled and their corresponding aeroelastic ROMs constructed and stored in the offline phase in a database $\mathcal{DB}$. These points correspond to a lattice $(M_\infty, f) \in \{0.6, 0.75, 0.9, 0.95, 1.0, 1.05, 1.1\} \times \{0, 50, 100\}$. For each operating point, a structural ROM of dimension $k^{(s)} = 4$ is constructed by projecting

the linear structural HDM onto its first four natural modes. Then a fluid ROM of dimension $k^{(f)} = 15$ is constructed by POD using the approach described in [10, 11, 18] and a reduction of the system in descriptor form [25]. The FSIs predicted by those 21 aeroelastic ROMs are reported in the right portion of Figure 9. Very good agreements can be observed at the database points when compared to their counterparts determined by the HDM that are depicted in the left portion of that same figure.

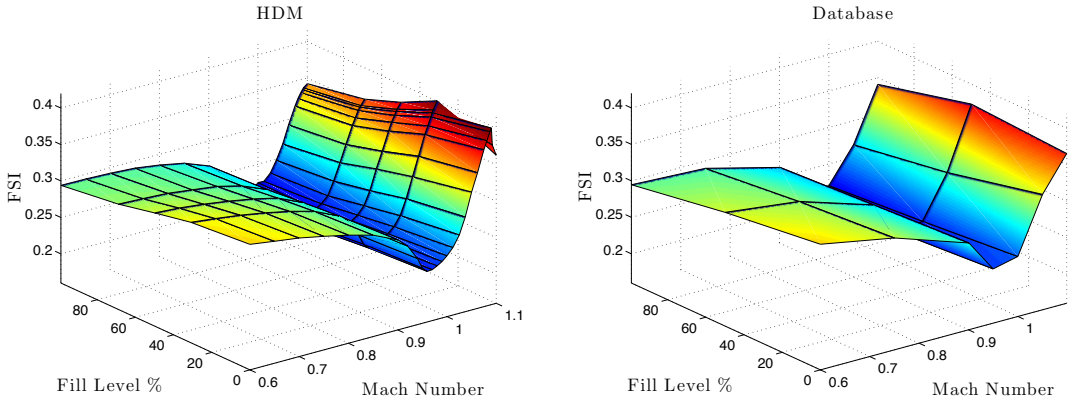

Figure 9 Comparison of the high-dimensional model and database reduced-order models flutter speed indices.

The 21 pre-computed aeroelastic ROMs are then distributed in $N_s = 3$ sub-databases: the first one covers the subsonic and lower transonic flow regime $M_\infty \in [0.6, 0.9]$, the second one the upper transonic regime $M_\infty \in [0.9, 1.0]$ and the third one the supersonic regime $M_\infty \in [1.0, 1.1]$. These three databases are graphically depicted in Figure 10. In the online interpolation procedure, in each database, piecewise-linear interpolation will be used in the M_∞ direction and cubic spline interpolation in the f direction.

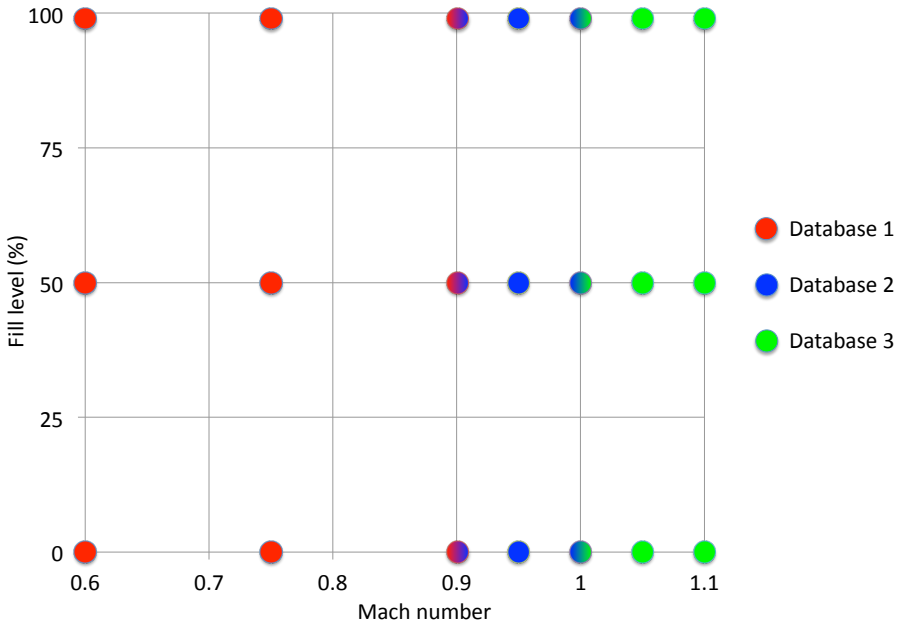

Figure 10 Pre-computed sub-databases $\{\mathcal{DB}_s\}_{s=1}^3$ of aeroelastic reduced-order models.

Before the online phase, the heuristic developed in [19] and mentioned in Section 4.1 is applied for choosing the manifold onto which to interpolate the reduced fluid operators. For the fluid operators, interpolation can indeed be done on the manifold $\mathrm{GL}\left(k^{(f)}\right)$ of non-singular matrices of size $k^{(f)}$ or on $\mathbb{R}^{k^{(f)}\times k^{(f)}}$. Since the interpolation procedure of choice involves two points in the M_∞ direction and three in the f direction at a time, the heuristic is applied for six different regions of the parametric space, as indicated in Table 3. As reported in Table 3, the manifold $\mathrm{GL}\left(k^{(f)}\right)$ is chosen in two regions while the manifold $\mathbb{R}^{k^{(f)}\times k^{(f)}}$ is chosen in four regions.

	Database 1		Database 2		Database 3	
$M_\infty \in$	$[0.6, 0.75]$	$[0.75, 0.9]$	$[0.9, 0.95]$	$[0.95, 1]$	$[1, 1.05]$	$[1.05, 1.1]$
$\mathrm{GL}\left(k^{(f)}\right)$	0.89	0.87	0.93	0.93	0.76	0.86
$\mathbb{R}^{k^{(f)}\times k^{(f)}}$	0.84	0.86	0.98	0.87	0.78	0.82
Manifold choice	$\mathbb{R}^{k^{(f)}\times k^{(f)}}$	$\mathbb{R}^{k^{(f)}\times k^{(f)}}$	$\mathrm{GL}\left(k^{(f)}\right)$	$\mathbb{R}^{k^{(f)}\times k^{(f)}}$	$\mathrm{GL}\left(k^{(f)}\right)$	$\mathbb{R}^{k^{(f)}\times k^{(f)}}$

Table 3 Non-linearity indicator in each database for the manifold choice heuristic

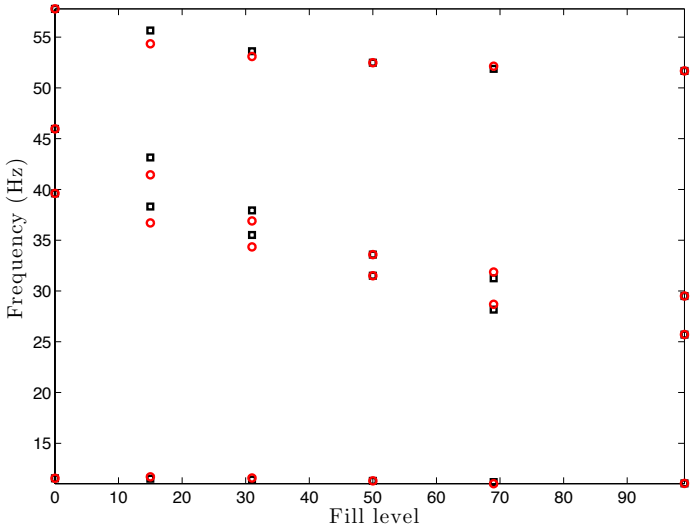

Figure 11 Comparison of eigenvalues of the structural subsystem: HDM □, interpolated ROM ○.

Next, the proposed methodology is applied to interpolate the aeroelastic ROM operators. The properties of the structural operators resulting from that interpolation are first analyzed by comparing their respective eigenfrequencies to their HDM counterparts. The corresponding results are reported in Figure 11. Good agreements can be observed, even for fill levels that are not present in the database. Next, the interpolated aeroelastic ROM operators are used to predict the onset of flutter in the entire parametric domain $(M_\infty, f) \in [0.6, 1.1] \times [0, 100]$. The predicted FSIs are reported in Figure 12. Very good qualitative and quantitative agreement can be observed for all flight conditions considered. For comparison, response surface estimation (RSE) is also applied to predict flutter using the database FSI data reported in the right portion of Figure 9. In this case, bicubic spline interpolation is used. When compared with the predictions arising from ROM interpolation, the results from RSE are found to be much less accurate, especially near the transonic dip and in the supersonic regime. RSE cannot, in particular, predict the FSI behavior for low fill levels at supersonic speeds. It is quite remarkable that the method proposed in this paper can capture this complex phenomenon with only the ROM database associated with the results shown in the right portion of Figure 9.

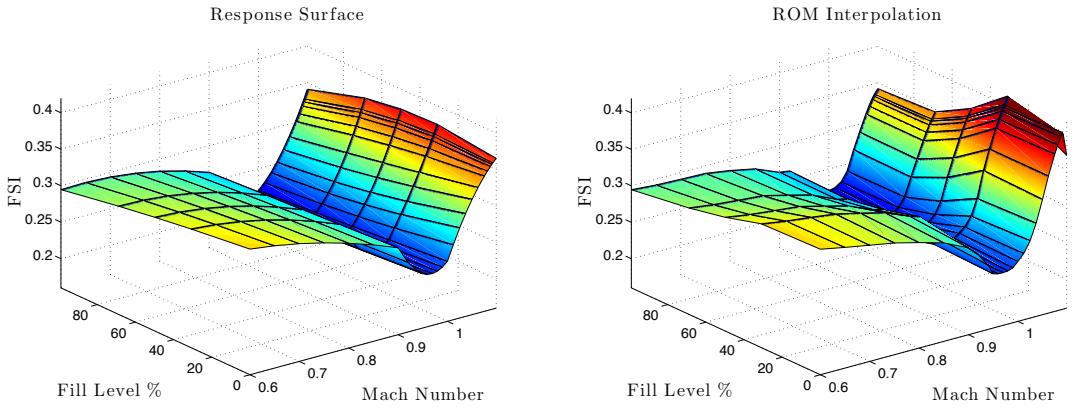

Figure 12 Comparison of flutter speed indices predicted using (1) response surface estimation, (2) ROM interpolation.

This example underlines the potential for accurate predictions of the proposed method which operates by interpolating models and not outputs, as in RSE. The offline and online CPU times associated with the prediction of the entire parametric FSI surface each of the four techniques are reported in Table 4. These results clearly demonstrate the real-time capability of the proposed approach, as it can accurately predict the FSI for 130 configurations in only 31 seconds.

Approach	Offline phase		Online phase	
	Wall time (s)	Number of processors	Wall time (s)	Number of processors
HDM	-	-	9,152,000	32
RSE	28,000	32	2	1
ROM database	28,000	32	31	1

Table 4 Wall times associated with computing the complete predicted FSI surface reported in Figure 9 and 12

The flutter behavior at supersonic speed for low fuel levels is then studied more in detail by predicting the FSI at an additional fuel level for 15% tank fill. The corresponding FSI are reported in Figure 13. In order to understand the physical phenomenon at play, the eigenvalues of the interpolated aeroelastic ROM matrices are computed for increasing values of free-stream pressure until flutter is reached. By following the wet structural modes in the complex plane, one can determine which structural mode flutters, that is which one is the first to cross the imaginary axis. Results are reported in Figures 14 and 15 for four different values of the free-stream mach number and an empty tank. One can observe that for $M_\infty = 1.075$ and $M_\infty = 1.091$, the first mode is the first to cross the imaginary axis while for $M_\infty = 1.092$ and $M_\infty = 1.1$, the third mode is the first one to flutter. These results clearly show that a bifurcation phenomenon is at play. Being able to perform such analyses demonstrates another clear advantage of the proposed method over RSE. For that same fill level, the HDM predicts the same phenomenon, that is a peak of FSI in function of the free-stream Mach number M_∞ between $M_\infty = 1.09$ and $M_\infty = 1.092$, which is in perfect agreement with the results arising from the interpolated ROM.

Next, the effect of the manifold choice heuristic is studied by considering interpolation on $\mathbb{R}^{k^{(f)} \times k^{(f)}}$ and on $\mathrm{GL}(k^{(f)})$, respectively, for the reduced fluid operator at every operating point. The corresponding results are reported in Figure 16 for interpolation using Choice 1 and 3, respectively. One can observe that the predicted FSI are more accurate when the heuristic is used, especially for subsonic and transonic flight conditions.

Finally, the effect of consistency on the results accuracy is investigated. Inconsistent interpolation for both the structural and fluid subsystems and for only one of those two subsystems is performed and the

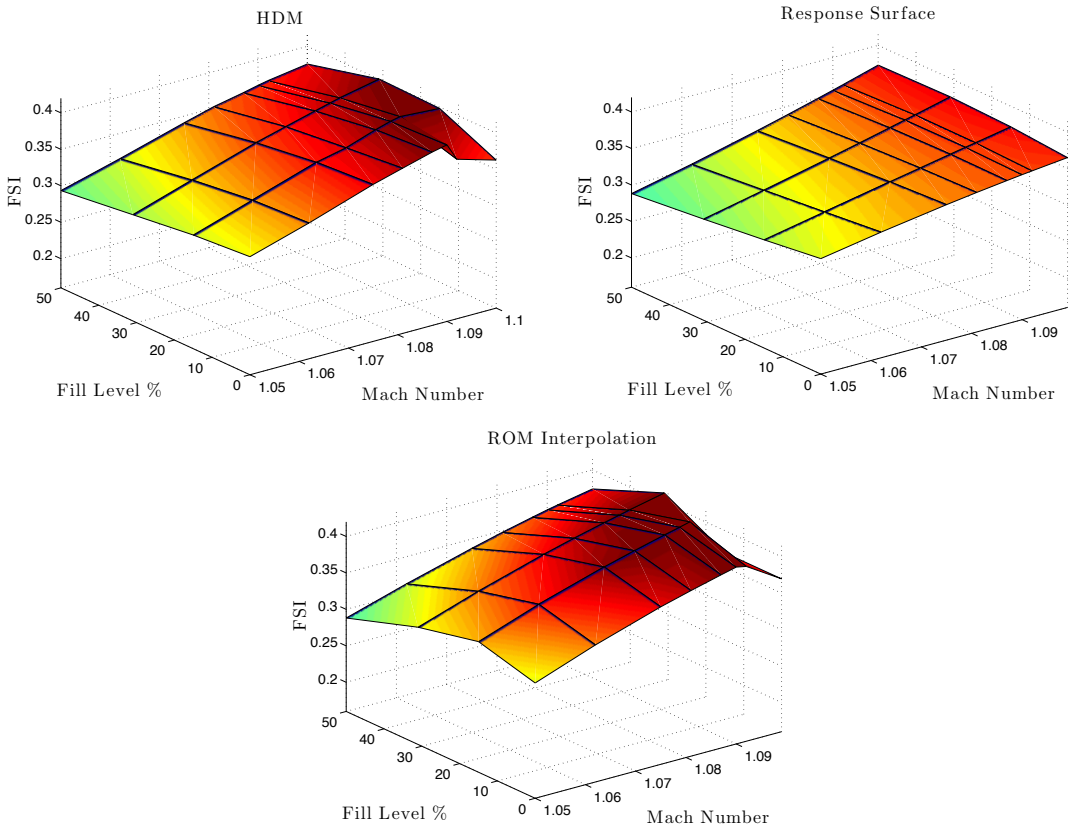

Figure 13 Comparison of high-dimensional model and predicted flutter speed indices between $M_\infty = 1.05$ and $M_\infty = 1.1$ for low fuel fill levels using (1) response surface estimation, (2) ROM interpolation

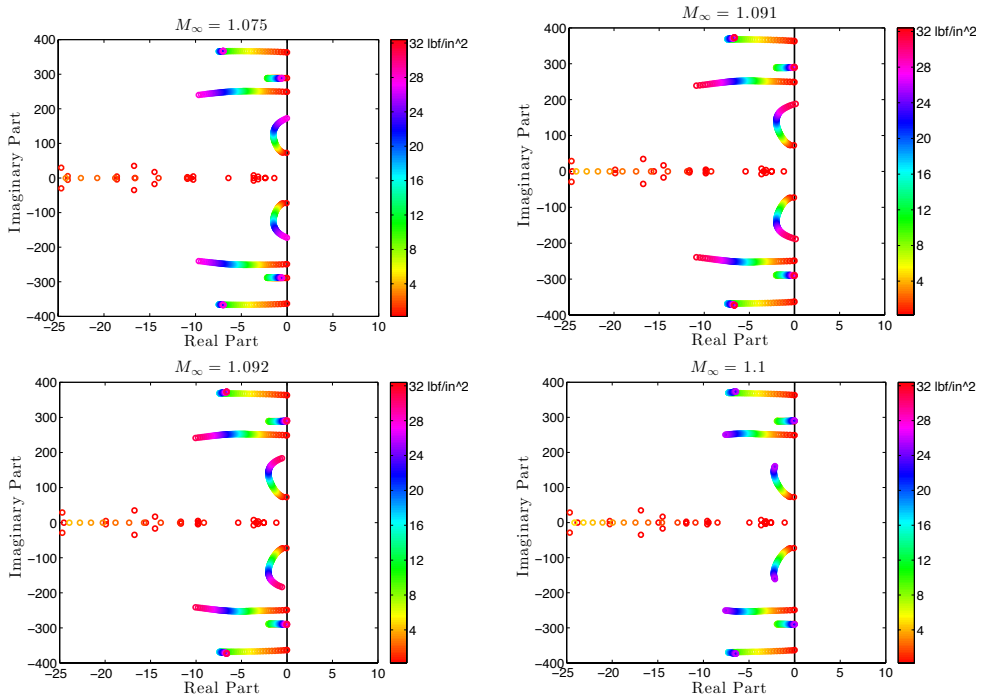

Figure 14 Aeroelastic matrix eigenvalues loci at 0% fill level for various free-stream Mach numbers.

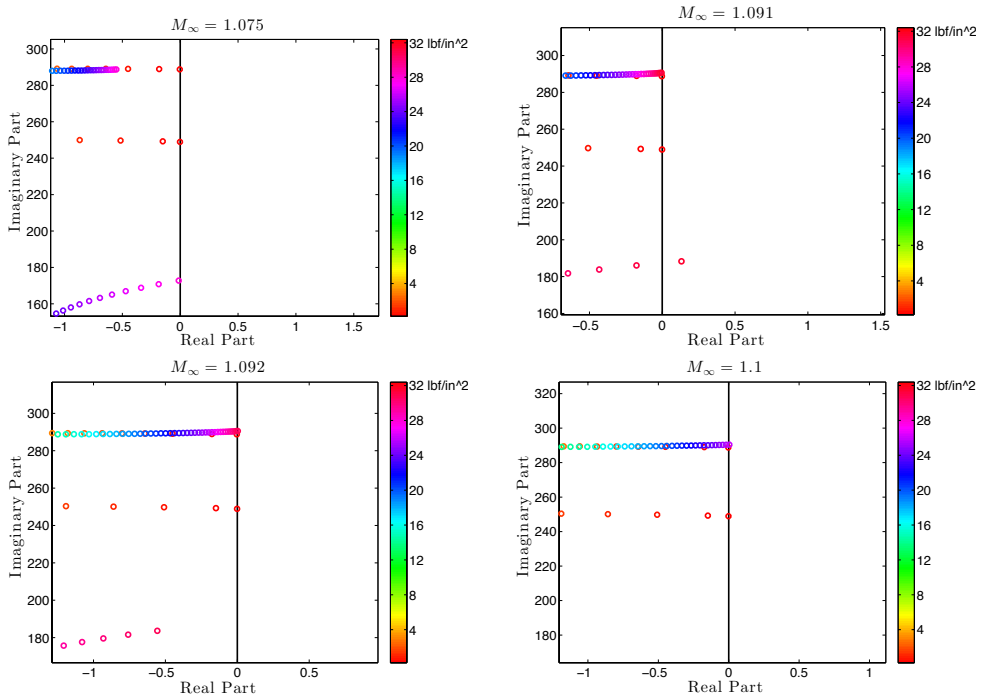

Figure 15 Aeroelastic matrix eigenvalues loci at 0% fill level for various free-stream Mach numbers (zoom).

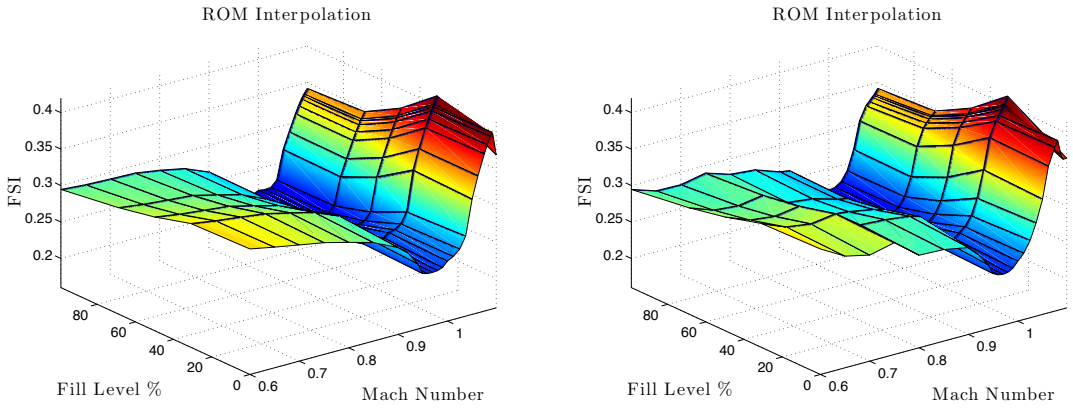

Figure 16 Predicted flutter speed indices using ROM interpolation without the manifold choice heuristic: interpolation of the reduced fluid operator on $\mathbb{R}^{k^{(f)} \times k^{(f)}}$ (left) and on $\mathrm{GL}(k^{(f)})$ (right).

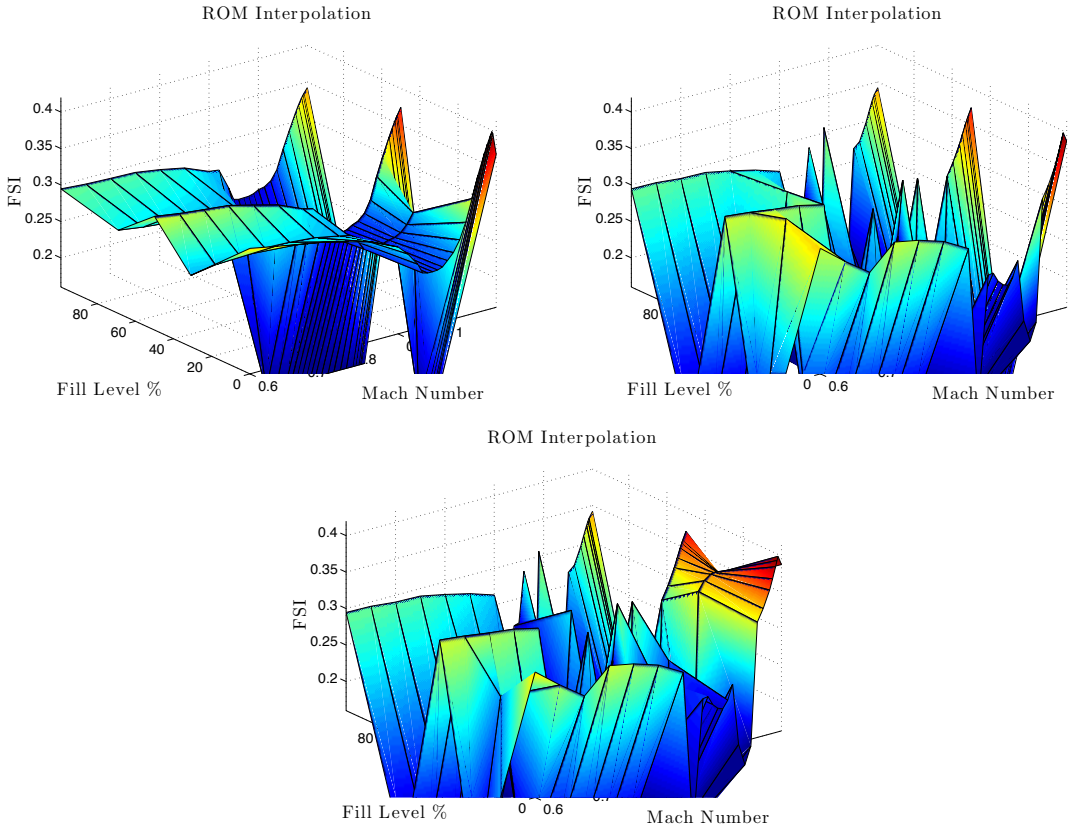

Figure 17 Predicted flutter speed indices using ROM interpolation without consistency enforcement: for the structural operators only (top left), for the fluid operators only (top right), for all operators (bottom).

corresponding FSI results reported in Figure 17. The reader can observe the crucial effect of consistency as none of the interpolation of inconsistent ROMs leads to accurate predicted FSI.

The interpolated ROM can also be used to predict the displacement at a given location of the wing-tank system. Here wing tip displacements time histories are predicted using the interpolated ROM at the transonic tip, that is $M_\infty = 0.97$ for an empty tank. The corresponding results are reported in Figure 18 for three different cruise altitudes, and compared to predictions using the HDM. Good agreements can be observed.

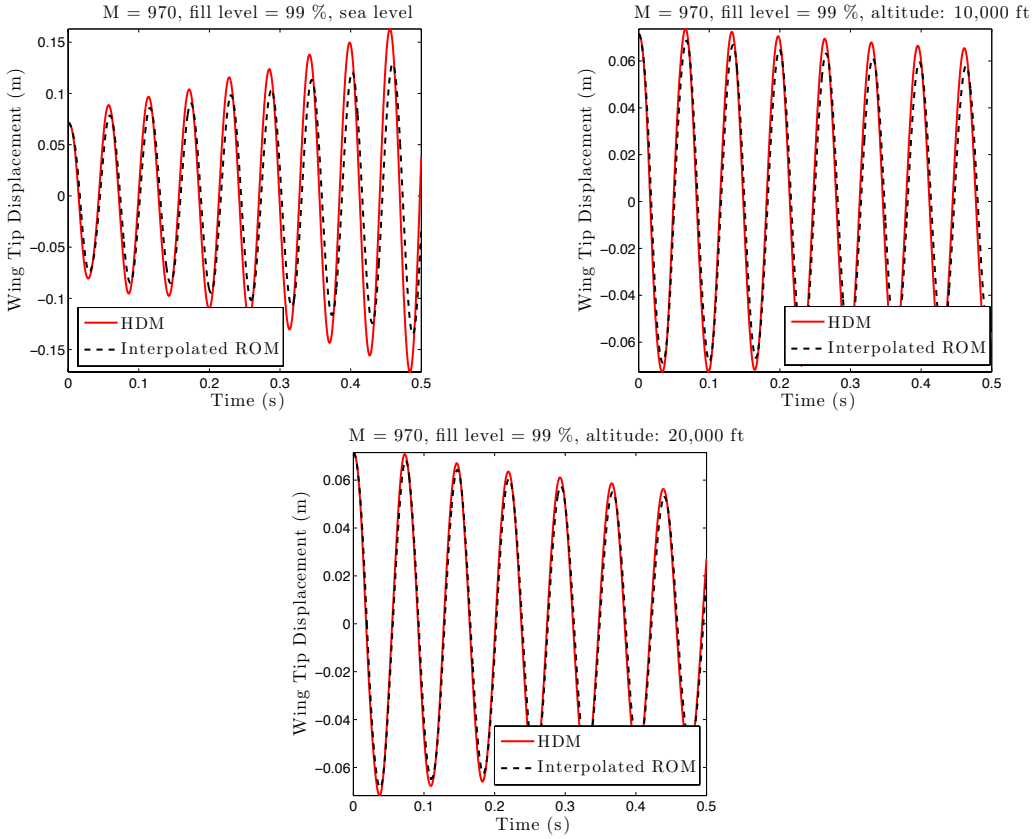

Figure 18 Wing tip displacement at $M_\infty = 0.97$ with full tank predicted using the high-dimensional model and an interpolated ROM at various altitudes.

Finally, in order to demonstrate the capability of the proposed method to operate on mobile devices, an iPhone application is implemented for the aeroelastic system of interest. A screenshot of the application is displayed in Figure 19. The application can operate in the following two modes, based on the database of $N_{\text{DB}} = 21$ points considered in this section: (1) In the first mode, for a given value of the fill level f, the FSI is compiled for $M_\infty \in [0.6, 1.1]$. This is the mode depicted in Figure 19. (2) In the second mode, for a given combination (M_∞, f), the smallest aeroelastic damping ratio is computed for the altitude range $h \in [0, 40000]$ ft.

6. Conclusions

This work presents a framework for real-time predictions based on a database of linear reduced-order models. It is based on the offline pre-computation of reduced-order models and their online interpolation at unsampled values of the parameters. A pre-processing step is first established to enforce the consistency of the set of generalized coordinates each reduced operator is defined by. The present paper presents such

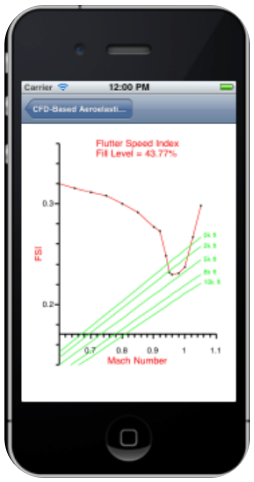

Figure 19 Screenshot of the iPhone application depicting the FSI for fill level $f = 43.77\%$.

a step for both systems defined on common and arbitrary underlying meshes. The operators are then interpolated on the tangent space to a matrix manifold to enforce properties associated with each operator. The framework is then applied to two challenging multi-physics applications, demonstrated its capability to lead to real-time and accurate predictions.

7. Acknowledgements

The authors would like to thank Mark Potts for the implementation of the iPhone application. The authors acknowledge partial support by the Army Research Laboratory through the Army High Performance Computing Research Center under Cooperative Agreement W911NF-07-2-0027, and partial support by the Office of Naval Research under grants no. N00014-11-1-0707 and N00014-14-1-0233. This document does not necessarily reflect the position of these institutions, and no official endorsement should be inferred.

8. Appendix 1: proof of Theorem 1

The objective function can be written as

$$\mathcal{J}_G(\mathbf{Q}) = \epsilon\langle \mathbf{Q}^T\mathbf{E}_{ri}\mathbf{Q}, \mathbf{E}_r^0\rangle + \alpha\langle \mathbf{Q}^T\mathbf{A}_{ri}\mathbf{Q}, \mathbf{A}_r^0\rangle + \langle \mathbf{F}, \mathbf{Q}\rangle, \tag{51}$$

where $\mathbf{F} = \beta\mathbf{B}_{ri}\left(\mathbf{B}_r^0\right)^T + \gamma\mathbf{C}_{ri}^T\mathbf{C}_r^0$.

The Lagrangian of the optimization problem is then

$$\begin{aligned}\mathcal{L}(\mathbf{Q},\mathbf{S}) &= \mathcal{J}_G(\mathbf{Q}) + \left\langle \frac{1}{2}\mathbf{S}, \mathbf{I}_k - \mathbf{Q}^T\mathbf{Q}\right\rangle \\ &= \epsilon\langle \mathbf{Q}^T\mathbf{E}_{ri}\mathbf{Q}, \mathbf{E}_r^0\rangle + \alpha\langle \mathbf{Q}^T\mathbf{A}_{ri}\mathbf{Q}, \mathbf{A}_r^0\rangle + \langle \mathbf{F}, \mathbf{Q}\rangle + \left\langle \frac{1}{2}\mathbf{S}, \mathbf{I}_k - \mathbf{Q}^T\mathbf{Q}\right\rangle,\end{aligned} \tag{52}$$

where $\frac{1}{2}\mathbf{S} \in \mathbb{R}^{k\times k}$ is a symmetric matrix of Lagrangian multipliers. Using the following identities [26],

$$\nabla_{\mathbf{Q}}\langle \mathbf{M}, \mathbf{Q}\rangle = \mathbf{M} \tag{53}$$

$$\nabla_{\mathbf{Q}}\langle \mathbf{M}, \mathbf{Q}^T\mathbf{Q}\rangle = \mathbf{Q}(\mathbf{M} + \mathbf{M}^T) \tag{54}$$

$$\nabla_{\mathbf{Q}}\langle \mathbf{Q}^T\mathbf{M}\mathbf{Q}, \mathbf{N}\rangle = \mathbf{M}\mathbf{Q}\mathbf{N}^T + \mathbf{M}^T\mathbf{Q}\mathbf{N}, \tag{55}$$

the gradient of the Lagrangian with respect to $\mathbf{Q}$ is obtained as

$$\nabla_{\mathbf{Q}}\mathcal{L}(\mathbf{Q},\mathbf{S}) = \epsilon\left(\mathbf{E}_{ri}\mathbf{Q}\left(\mathbf{E}_r^0\right)^T + \mathbf{E}_{ri}^T\mathbf{Q}\mathbf{E}_r^0\right) + \alpha\left(\mathbf{A}_{ri}\mathbf{Q}\left(\mathbf{A}_r^0\right)^T + \mathbf{A}_{ri}^T\mathbf{Q}\mathbf{A}_r^0\right) + \mathbf{F} - \mathbf{Q}\mathbf{S} \tag{56}$$

which leads to the first-order optimality condition

$$\mathbf{Q}\mathbf{S} = \epsilon\left(\mathbf{E}_{ri}\mathbf{Q}\left(\mathbf{E}_r^0\right)^T + \mathbf{E}_{ri}^T\mathbf{Q}\mathbf{E}_r^0\right) + \alpha\left(\mathbf{A}_{ri}\mathbf{Q}\left(\mathbf{A}_r^0\right)^T + \mathbf{A}_{ri}^T\mathbf{Q}\mathbf{A}_r^0\right) + \mathbf{F}, \tag{57}$$

together with the constraint $\mathbf{Q}^T\mathbf{Q} = \mathbf{I}_k$ and the property that $\mathbf{S}$ is symmetric.

9. Appendix 2: proof of Theorem 2

The goal of this section is to prove that the set of fixed points of the proposed recursive algorithm is equal to the set of critical points of the objective function $\mathcal{J}_G$.

Let $\widehat{\mathbf{Q}}$ denote a fixed point of the recursive method defined in Algorithm 2. Then $\widehat{\mathbf{Q}}$ satisfies $\widehat{\mathbf{Q}} = \widehat{\mathbf{U}}\widehat{\mathbf{V}}^T$ where

$$\widehat{\mathbf{U}}\widehat{\mathbf{\Sigma}}\widehat{\mathbf{V}}^T = \epsilon\left(\mathbf{E}_{ri}\widehat{\mathbf{Q}}\left(\mathbf{E}_r^0\right)^T + \mathbf{E}_{ri}^T\widehat{\mathbf{Q}}\mathbf{E}_r^0\right) + \alpha\left(\mathbf{A}_{ri}\widehat{\mathbf{Q}}\left(\mathbf{A}_r^0\right)^T + \mathbf{A}_{ri}^T\widehat{\mathbf{Q}}\mathbf{A}_r^0\right) + s\widehat{\mathbf{Q}}\mathbf{F} \tag{58}$$

is a singular value decomposition. Since $\widehat{\mathbf{V}}$ is an orthogonal matrix,

$$\widehat{\mathbf{U}}\widehat{\mathbf{V}}^T\widehat{\mathbf{V}}\widehat{\mathbf{\Sigma}}\widehat{\mathbf{V}}^T = \epsilon\left(\mathbf{E}_{ri}\widehat{\mathbf{Q}}\left(\mathbf{E}_r^0\right)^T + \mathbf{E}_{ri}^T\widehat{\mathbf{Q}}\mathbf{E}_r^0\right) + \alpha\left(\mathbf{A}_{ri}\widehat{\mathbf{Q}}\left(\mathbf{A}_r^0\right)^T + \mathbf{A}_{ri}^T\widehat{\mathbf{Q}}\mathbf{A}_r^0\right) + s\widehat{\mathbf{Q}} + \mathbf{F}, \tag{59}$$

that is

$$\widehat{\mathbf{Q}}\mathbf{S} = \epsilon\left(\mathbf{E}_{ri}\widehat{\mathbf{Q}}\left(\mathbf{E}_r^0\right)^T + \mathbf{E}_{ri}^T\widehat{\mathbf{Q}}\mathbf{E}_r^0\right) + \alpha\left(\mathbf{A}_{ri}\widehat{\mathbf{Q}}\left(\mathbf{A}_r^0\right)^T + \mathbf{A}_{ri}^T\widehat{\mathbf{Q}}\mathbf{A}_r^0\right) + \mathbf{F}, \tag{60}$$

where $\mathbf{S} = \widehat{\mathbf{V}}\widehat{\mathbf{\Sigma}}\widehat{\mathbf{V}}^T - s\mathbf{I}_k$ is a symmetric matrix. $\widehat{\mathbf{U}}$ and $\widehat{\mathbf{V}}$ being orthogonal, $\widehat{\mathbf{Q}}$ is orthogonal as well and therefore meets the requirements of Theorem 2. The set of fixed points of Algorithm 2 is included in the set of critical point of $\mathcal{J}_G$.

Conversely, let $\mathbf{Q}^\star$ be a critical point of $\mathcal{J}_G$. Then, there exists a symmetric matrix $\mathbf{S}$ such that Eq. (34) holds with $\mathbf{Q}^\star$ orthogonal. Since, $\mathbf{S}$ is real and symmetric, it is diagonalizable as

$$\mathbf{S} = \mathbf{U}\mathbf{\Lambda}\mathbf{U}^T, \tag{61}$$

the eigenvalues in $\mathbf{\Lambda}$ being real and ordered decreasingly and $\mathbf{U}$ an orthogonal matrix. Then,

$$\mathbf{Q}^\star\mathbf{U}\mathbf{\Lambda}\mathbf{U}^T + s\mathbf{Q}^\star = \epsilon\left(\mathbf{E}_{ri}\mathbf{Q}^\star\left(\mathbf{E}_r^0\right)^T + \mathbf{E}_{ri}^T\mathbf{Q}^\star\mathbf{E}_r^0\right) + \alpha\left(\mathbf{A}_{ri}\mathbf{Q}^\star\left(\mathbf{A}_r^0\right)^T + \mathbf{A}_{ri}^T\mathbf{Q}^\star\mathbf{A}_r^0\right) + \mathbf{F} + s\mathbf{Q}^\star \tag{62}$$

which can also be written as

$$(\mathbf{Q}^\star\mathbf{U})(\mathbf{\Lambda} + s\mathbf{I})\mathbf{U}^T = \epsilon\left(\mathbf{E}_{ri}\mathbf{Q}^\star\left(\mathbf{E}_r^0\right)^T + \mathbf{E}_{ri}^T\mathbf{Q}^\star\mathbf{E}_r^0\right) + \alpha\left(\mathbf{A}_{ri}\mathbf{Q}^\star\left(\mathbf{A}_r^0\right)^T + \mathbf{A}_{ri}^T\mathbf{Q}^\star\mathbf{A}_r^0\right) + s\mathbf{Q}^\star + \mathbf{F}. \tag{63}$$

In order to conclude the proof, it remains to show that $(\mathbf{Q}^\star\mathbf{U})(\mathbf{\Lambda} + s\mathbf{I})\mathbf{U}^T$ is a singular value decomposition. $\mathbf{Q}^\star\mathbf{U}$ and $\mathbf{U}$ being orthogonal matrices, and $\mathbf{\Lambda} + s\mathbf{I}$ being a diagonal matrix, it is sufficient to show that $\mathbf{\Lambda} + s\mathbf{I}$ has all diagonal positive entries.

From Eq. (62),

$$\|\mathbf{\Lambda}\|_2 = \left\|\mathbf{Q}^\star\mathbf{U}\mathbf{\Lambda}\mathbf{U}^T\right\|_2 = \left\|\epsilon\left(\mathbf{E}_{ri}\mathbf{Q}^\star\left(\mathbf{E}_r^0\right)^T + \mathbf{E}_{ri}^T\mathbf{Q}^\star\mathbf{E}_r^0\right) + \alpha\left(\mathbf{A}_{ri}\mathbf{Q}^\star\left(\mathbf{A}_r^0\right)^T + \mathbf{A}_{ri}^T\mathbf{Q}^\star\mathbf{A}_r^0\right) + \mathbf{F}\right\|_2, \tag{64}$$

and

$$\begin{aligned}
\|\mathbf{\Lambda}\|_2 &\leq \epsilon\left\|\mathbf{E}_{ri}\mathbf{Q}^\star\left(\mathbf{E}_r^0\right)^T + \mathbf{E}_{ri}^T\mathbf{Q}^\star\mathbf{E}_r^0\right\|_2 + \alpha\left\|\mathbf{A}_{ri}\mathbf{Q}^\star\left(\mathbf{A}_r^0\right)^T + \mathbf{A}_{ri}^T\mathbf{Q}^\star\mathbf{A}_r^0\right\|_2 + \|\mathbf{F}\|_2 \\
&\leq \epsilon\left(\|\mathbf{E}_{ri}\|_2\|\mathbf{Q}^\star\|_2\left\|\left(\mathbf{E}_r^0\right)^T\right\|_2 + \|\mathbf{E}_{ri}^T\|_2\|\mathbf{Q}^\star\|_2\|\mathbf{E}_r^0\|_2\right) \\
&\quad + \alpha\left(\|\mathbf{A}_{ri}\|_2\|\mathbf{Q}^\star\|_2\left\|\left(\mathbf{A}_r^0\right)^T\right\|_2 + \|\mathbf{A}_{ri}^T\|_2\|\mathbf{Q}^\star\|_2\|\mathbf{A}_r^0\|_2\right) + \|\mathbf{F}\|_2 \\
&\leq 2\epsilon\|\mathbf{E}_{ri}\|_2\|\mathbf{E}_r^0\|_2 + 2\alpha\|\mathbf{A}_{ri}\|_2\|\mathbf{A}_r^0\|_2 + \|\mathbf{F}\|_2 \\
&\leq s_{\min,\mathrm{G}}
\end{aligned} \tag{65}$$

by definition of $s_{\min,\mathrm{G}}$ in Eq. (30). Denoting by λ_i $i = 1, \cdots, k$ the diagonal entries in $\mathbf{\Lambda}$, this implies that

$$-s_{\min,\mathrm{G}} \leq \lambda_i \leq s_{min,G},\ i = 1, \cdots, k, \tag{66}$$

and, since $s > s_{\min,\mathrm{G}}$,

$$\lambda_i + s > 0,\ i = 1, \cdots, k. \tag{67}$$

The set of critical points of $\mathcal{J}_G$ is included in the set of fixed points of Algorithm 2 and the two sets are equal, concluding the proof.

References

References

[1] B. Moore, Principal component analysis in linear systems: Controllability, observability, and model reduction, IEEE Transactions on Automatic Control 26 (1981) 17–32.

[2] L. Sirovich, Turbulence and the dynamics of coherent structures. Part I: coherent structures, Quarterly of applied mathematics 45 (1987) 561–571.

[3] D. Ryckelynck, A priori hyperreduction method: an adaptive approach, Journal of Computational Physics 202 (2005) 346–366.

[4] S. Chaturantabut, D. Sorensen, Nonlinear model reduction via discrete empirical interpolation, SIAM Journal on Scientific Computing 32 (2010) 2737–2764.

[5] K. Carlberg, C. Bou-Mosleh, C. Farhat, Efficient non-linear model reduction via a least-squares Petrov–Galerkin projection and compressive tensor approximations, International Journal for Numerical Methods in Engineering 86 (2011) 155–181.

[6] D. Amsallem, M. J. Zahr, C. Farhat, Nonlinear model order reduction based on local reduced-order bases, International Journal for Numerical Methods in Engineering 92 (2012) 891–916.

[7] K. Carlberg, C. Farhat, J. Cortial, D. Amsallem, The GNAT method for nonlinear model reduction: effective implementation and application to computational fluid dynamics and turbulent flows, Journal of Computational Physics 242 (2013) 623–647.

[8] C. Farhat, P. Avery, T. Chapman, J. Cortial, Dimensional reduction of nonlinear finite element dynamic models with finite rotations and energy-based mesh sampling and weighting for computational efficiency, International Journal for Numerical Methods in Engineering 98 (2014) 625–662.

[9] K. Veroy, A. T. Patera, Certified real-time solution of the parametrized steady incompressible Navier-Stokes equations: rigorous reduced-basis a posteriori error bounds, International Journal for Numerical Methods in Fluids 47 (2005) 773–788.

[10] D. Amsallem, C. Farhat, Interpolation method for adapting reduced-order models and application to aeroelasticity, AIAA Journal 46 (2008) 1803–1813.

[11] D. Amsallem, J. Cortial, C. Farhat, Toward real-time computational-fluid-dynamics-based aeroelastic computations using a database of reduced-order information, AIAA Journal 48 (2010) 2029–2037.

[12] F. Negri, A. Manzoni, D. Amsallem, Efficient model reduction of parametrized systems by matrix discrete empirical interpolation, Submitted for publication (2015).

[13] A. Paul-Dubois-Taine, D. Amsallem, An adaptive and efficient greedy procedure for the optimal training of parametric reduced-order models, International Journal for Numerical Methods in Engineering 102 (2015) 1262–1292.

[14] D. Amsallem, M. J. Zahr, Y. Choi, C. Farhat, Design Optimization Using Hyper-Reduced-Order Models, Structural and Multidisciplinary Optimization 51 (2015) 919–940.

[15] D. Amsallem, M. J. Zahr, K. Washabaugh, Fast Local Reduced Basis Updates for the Efficient Reduction of Nonlinear Systems with Hyper-Reduction , Special issue on Model Reduction of Parameterized Systems (MoRePaS), Advances in Computational Mathematics (2015) 1–34.

[16] Y. Wu, U. Hetmaniuk, Adaptive training of local reduced bases for unsteady incompressible Navier-Stokes flows, International Journal for Numerical Methods in Engineering, published online (2015) 1–22.

[17] D. Amsallem, J. Cortial, K. Carlberg, C. Farhat, A method for interpolating on manifolds structural dynamics reduced-order models, International Journal for Numerical Methods in Engineering 80 (2009) 1241–1258.

[18] D. Amsallem, Interpolation on Manifolds of CFD-Based Fluid and Finite Element-Based Structural Reduced-Order Models for On-Line Aeroelastic Predictions, Ph.D. thesis, Ph.D. Thesis, Stanford University, 2010.

[19] J. Degroote, J. Vierendeels, K. Willcox, Interpolation among reduced-order matrices to obtain parameterized models for design, optimization and probabilistic analysis, International Journal for Numerical Methods in Fluids 63 (2010) 207–230.

[20] H. Panzer, J. Mohring, R. Eid, B. Lohmann, Parametric Model Order Reduction by Matrix Interpolation, at-Automatisierungstechnik 58 (2010) 475–484.

[21] D. Amsallem, C. Farhat, An online method for interpolating linear parametric reduced-order models, SIAM Journal on Scientific Computing 33 (2011) 2169–2198.

[22] G. Berkooz, P. Holmes, J. L. Lumley, The proper orthogonal decomposition in the analysis of turbulent flows, Annual Review of Fluid Mechanics 25 (1993) 539–575.

[23] E. J. Grimme, Krylov projection methods for model reduction, Ph.D. thesis, Ph.D. Thesis, University of Illinois at Urbana Champaign, 1997.

[24] U. Hetmaniuk, R. Tezaur, C. Farhat, Review and assessment of interpolatory model order reduction methods for frequency response structural dynamics and acoustics problems, International Journal for Numerical Methods in Engineering 90 (2012) 1636–1662.

[25] D. Amsallem, C. Farhat, On the Stability of Reduced-Order Linearized Computational Fluid Dynamics Models Based on POD and Galerkin Projection: Descriptor vs Non-Descriptor Forms, volume 9, Reduced Order Methods for Modeling and Computational Reduction, MS&A - Modeling, Simulation and Applications, Springer, 2014.

[26] C. Fraikin, Y. Nesterov, P. V. Dooren, Optimizing the Coupling Between Two Isometric Projections of Matrices, SIAM Journal on Matrix Analysis and Applications 30 (2008) 324–345.

[27] U. Helmke, J. Barratt Moore, Optimization and Dynamical Systems, Springer, 1994.

[28] R. Zimmermann, A Locally Parametrized Reduced-Order Model for the Linear Frequency Domain Approach to Time-Accurate Computational Fluid Dynamics, SIAM Journal on Scientific Computing 36 (2014) B508–B537.

[29] Y. Choi, D. Amsallem, C. Farhat, Gradient-Based Constrained Optimization Using a Database of Linear Reduced-Order Models, submitted to Arxiv (2015) 1–21.

[30] M. A. Grepl, A. T. Patera, A posteriori error bounds for reduced-basis approximations of parametrized parabolic partial differential equations, ESAIM: Mathematical Modelling and Numerical Analysis 39 (2005) 157–181.

[31] T. Bui-Thanh, K. Willcox, O. Ghattas, Parametric reduced-order models for probabilistic analysis of unsteady aerodynamic applications, AIAA Journal 46 (2008) 2520–2529.

[32] D. Amsallem, U. Hetmaniuk, A posteriori error estimators for linear reduced order models using Krylov-based integrators, International Journal for Numerical Methods in Engineering 102 (2015) 1238–1261.

[33] D. Colton, R. Kress, Inverse acoustic and electromagnetic scattering theory, Springer, 2013.

[34] J. P. Berenger, A perfectly matched layer for the absorption of electromagnetic waves, Journal of Computational Physics 114 (1994) 185–200.

[35] E. K.-y. Chiu, C. Farhat, Effects of fuel slosh on flutter prediction, AIAA 2009-2682, 50th AIAA/ASME/ASCE/AHS/ASC Structures, Structural Dynamics, and Materials Conference (2009).

[36] C. Farhat, E. K.-y. Chiu, D. Amsallem, J.-S. Schotté, R. Ohayon, Modeling of Fuel Sloshing and its Physical Effects on Flutter, AIAA Journal 51 (2013) 2252–2265.

[37] E. C. Yates, AGARD Standard Aeroelastic Configurations For Dynamic Response - 1 - Wing 445.6, NASA, 1987.